

Why do inverse models disagree? A case study with two European CO₂ inversions

Saqr Munassar^{1,2}, Guillaume Monteil³, Marko Scholze³, Ute Karstens⁴, Christian Rödenbeck¹, Frank-Thomas Koch^{1,5}, Kai U. Totsche⁶, and Christoph Gerbig¹

¹Department of Biogeochemical Signals, Max-Planck Institute for Biogeochemistry, Jena, Germany

²Department of Physics, Faculty of Sciences, Ibb University, Ibb, Yemen

³Department of Physical Geography and Ecosystem Science, Lund University, Lund, Sweden

⁴ICOS Carbon Portal at Lund University, Lund, Sweden

⁵Meteorological Observatory Hohenpeissenberg, Deutscher Wetterdienst, Hohenpeissenberg, Germany

¹⁰Institute of Geoscience, Friedrich Schiller University, Jena, Germany

Correspondence to: Saqr Munassar (smunas@bgc-jena.mpg.de)

Abstract. We present an analysis of atmospheric transport impact on estimating CO₂ fluxes using two atmospheric inversion systems (CarboScope Regional (CSR) and LUMIA) over Europe ~~in~~ 2018. The main focus of this study is to quantify the dominant drivers of spread amid CO₂ estimates derived from atmospheric tracer inversions. The Lagrangian transport

¹⁵ models STILT and FLEXPART were used to assess the impact of mesoscale transport. The impact of lateral boundary conditions for CO₂ was assessed by ~~using two different estimates, from the global inversion systems CarboScope (TM3) and TM5-4DVAR.~~ CO₂ estimates calculated with an ensemble of eight inversions differing in the regional and global transport models, as well as the inversion systems show a relatively large spread for the annual ~~fluxes~~, ranging between -0.72 and 0.20 PgC yr⁻¹ ~~larger than the prior uncertainty of 0.47 PgC yr⁻¹~~. The discrepancies ~~in annual budget are primarily caused by~~

²⁰ ~~differences in the mesoscale transport model~~ (0.51 PgC yr⁻¹), in comparison with 0.23 and 0.10 (PgC yr⁻¹) that resulted from the far-field contributions and the inversion systems, respectively. Additionally, varying the mesoscale transport caused large discrepancies in spatial and temporal patterns, while changing the lateral boundary conditions lead to more homogeneous spatial and temporal impact. We further investigated the origin of the discrepancies between transport models. The meteorological forcing parameters (forecasts versus reanalysis obtained from ECMWF data products) used to drive the

²⁵ transport models are responsible for a small part of the differences in CO₂ estimates, but the largest impact seems to come from the ~~transport model schemes~~. Although a good convergence in the differences between the inversion systems was achieved by applying a strict protocol of using identical priors, and atmospheric datasets, there was a non-negligible impact arising from applying a different inversion system. Specifically, the choice of prior error structure accounted for a large part of system-to-system differences.

Deleted: Impact of atmospheric transport

Deleted: on

Deleted: flux estimates

Deleted: derived from the atmospheric tracer inversions

Deleted: for

Deleted: applying

Deleted: transport models TM3 and TM5.

Deleted: domain wide

Deleted:

Deleted: with a mean estimate of -0.29 PgC

Deleted: largest

Deleted: resulted from varying

Formatted: Superscript

Deleted: , which amounted to a difference of

Deleted: (

Deleted: models

Deleted: themselves

1 Introduction

Inverse modeling has been increasingly used to infer surface-atmosphere fluxes of carbon dioxide (CO₂), from observations of dry mole fractions made at spatiotemporal points across an observational network (Enting and Newsam, 1990; Bousquet et al., 1999). Reducing uncertainty in the flux estimates is, therefore, essential to reliably quantify the carbon budget

50 (Friedlingstein et al., 2022; Le Quéré et al., 2018) as well as to improve our understanding about the variability and trends of the carbon cycle over times at finer regional scales, in particular in response to the climate perturbation caused by the increase of anthropogenic emissions (Shi et al., 2021). The estimates obtained from atmospheric tracer inversions still demonstrate large deviations due to manifold sources of uncertainty such as using different data, inversion schemes, and atmospheric transport models (Baker et al., 2006; Gurney et al., 2016), either at global scales or, to a larger extent, at 55 regional scales. Although the global inversions can provide convergent estimations of the global carbon budgets, they are limited by the coarse resolution of atmospheric transport that may not allow for a realistic representation of the observations at complex mesoscale terrains. In turn, performing regional inversions with mesoscale transport models has offered a better opportunity to represent and make use of the dense measurements available at all the sites across regional domains (Broquet et al., 2013; Kountouris et al., 2018a; Lauvaux et al., 2016), specifically after the expanding coverage of data over large areas 60 in the recent years as has been established, for example, over Europe by the Integrated Carbon Observation System (ICOS).

Although CO₂ fluxes constrained by atmospheric data in the Bayesian inversion framework inherit a dominant spatial and temporal pattern from the atmospheric signal, the a-posteriori fluxes still suffer from a large spread when using different global and mesoscale transport models (Rivier et al., 2010).

As a first intercomparison between six regional inversions covering a wide range of system characteristics –e.g., prior fluxes, 65 inversion approaches, and transport models, the EUROCOM experiment (Monteil et al., 2020) suggested large spreads in posterior estimates over Europe, particularly over regions that are poorly constrained by atmospheric data. This, on the one hand, partly indicates the sensitivity of the a-posteriori estimates to the observations and to the a-priori models as explained in Munassar et al. (2022). On the other hand, inaccuracies in atmospheric transport (Schuh et al., 2019), far-field contributions, and the configurations of inversions are responsible for part of that spread. A further study suggests that 70 uncertainties in both transport and CO₂ fluxes contribute equally to the uncertainties in CO₂ dry mole fraction simulations, displaying similar temporal and spatial patterns (Chen et al., 2019).

The atmospheric transport relates the measured tracer concentration to its possible sources and sinks, which are adjusted in order to fit the modelled concentrations to observed data. However, inaccuracies in representing the real atmospheric dynamics by transport models lead to uncertainties in CO₂ flux estimates. This kind of errors can emerge from both 75 simplified parameterizations of real physics and model parameters themselves (Engelen, 2002). The atmospheric transport models rely on a mesoscale representation of air mass movements, which cannot completely reproduce the observed fine scale variability of tracer concentration, leading to the so-called representation error. As a result, inversions cannot solve for fluxes at a lower spatial and temporal resolutions than that of their transport model resulting in aggregation errors (Kaminski

Moved (insertion) [10]

Deleted: s

Moved (insertion) [9]

Deleted: A further study suggests that uncertainties in both transport and CO₂ fluxes contribute equally to the uncertainties in CO₂ dry mole fraction simulations, displaying similar temporal and spatial patterns (Chen et al., 2019).†

Deleted: An

Deleted: model is used to

Deleted: modeled

Deleted: the

Deleted: ation

Deleted: of

Deleted: the

Deleted: ransport model

Deleted: †

An

Deleted: ies

Deleted: Additionally

Deleted: ,

Deleted: , which leads to

et al., 2001). Additionally, atmospheric transport models are typically driven by meteorological data available from operational weather forecast models or reanalysis data optimised against observations and dynamical model forecasts. 100 However, such meteorological fields have uncertainties owing to errors and gaps in the observations and errors in the weather forecast models (Deng et al., 2017; Liu et al., 2011; Tolk et al., 2008).

As the lateral boundaries are provided from a global model run at lower resolution than the regional model (Davies, 2014), this leads to biases in CO₂ lateral concentrations and thus affects the inversion estimates (Chen et al., 2019). The information of providing boundary conditions to regional inversions is necessary to isolate the influence of far-field contributions before 105 performing the regional inversion. In Bayesian inversion setups, a proper information on prior error structures is also essential to determine the spatial pattern of the flux corrections based on the assumed error, especially at high spatial resolution inversions (Chevallier et al., 2012; Kountouris et al., 2015; Lauvaux et al., 2016). Therefore, the spatial pattern of flux corrections is dependent on the way the error covariance matrices are constructed, which can lead to large spatial discrepancies between the estimates from different inversion systems.

110 This study is dedicated to quantify the relative contributions of the differences in optimised fluxes resulting from varying: 1) atmospheric transport models, 2) lateral boundary conditions, and 3) inversion configurations on flux estimates, as the error contributions from each component to the inversions spread remain unclear in regional inversions, specifically at finer spatial scales over a continental domain such as Europe (Monteil et al., 2020; Petrescu et al., 2021; Thompson et al., 2020). We analysed results of posterior NEE estimated from the two inversion systems CarboScope-Regional, CSR, (Kountouris et 115 al., 2018b; Munassar et al., 2022) and LUMIA (Monteil and Scholze, 2021). Both inversions employ pre-computed sensitivities of atmospheric mole fractions to surface fluxes, so-called source-weight functions or “footprints”, via two Lagrangian transport models at regional scales, and make use of the two-step inversion approach established by Roedenbeck et al. (2009) to provide the lateral boundary conditions. The regional atmospheric transport models were used at a horizontal resolution of 0.25-degree. The impacts of both global and regional models were compared through analysing the differences 120 in space and time.

Section 2 presents detailed descriptions of the inversion setups, the transport models, and the prior fluxes used. The observational stations that provide CO₂ dry mole fraction are described within the methods as well. We introduce the results obtained from eight inversions in Section 3. The results are discussed and interpreted through a spatial and temporal analysis 125 of the differences between the elements of inversions in Section 4. Finally, Section 5 highlights a few concluding remarks on the impacts of regional transport, boundary conditions and inversion setups on CO₂ estimates in the inverse modeling.

2 Methods

An atmospheric tracer inversion framework is mainly made up of transport model, data source for boundary conditions (in case of regional inversions), datasets of atmospheric mole fractions, and surface flux fields. In this study, several inversion runs differing in atmospheric transport models are conducted using two tracer inversion systems, CSR and LUMIA (see

Moved (insertion) [8]

Deleted: The accuracy of a

Deleted: typically

Deleted: depends

Deleted:

Deleted: upon the accuracy of meteorological data, since transport models are forced by meteorological parameters. ...

Moved up [7]: Tolk et al. (2008) also found meteorology to be a key driver of representation error, which varies spatially and temporally. They indicated that a large contribution to representation error is caused by unresolved model topography at coarse spatial resolution during night, but that convective structures, mesoscale circulations, and the variability of CO₂ fluxes dominate during daytime.¶

Moved up [8]: The accuracy of atmospheric transport models upon the accuracy of meteorological data, since transport models are forced by meteorological parameters. Deng et al. (2017) found that assimilating meteorological observations such as wind speed and wind direction in transport models significantly improved the model performances achieving an uncertainty reduction of about 50% in wind speed and direction, especially when measurements in the Planetary Boundary Layer (PBL) were assimilated. However, they concluded that the differences in CO₂ emissions reached up to 15% at local scale corrections after inversion and were limited to 5% for the total emissions integrated across the regional domain of interest. A further study suggests that uncertainties in both transport and CO₂ fluxes contribute equally to the uncertainties in CO₂ dry mole fraction

Moved up [9]: A further study suggests that uncertainties in both transport and CO₂ fluxes contribute equally to the uncertainties in

Moved (insertion) [7]

Deleted: (Liu et al., 2011; Deng et al., 2017; Tolk et al., 2008)Deng et al. (2017) found that assimilating meteorological observati... [1]

Formatted: Subscript

Moved up [10]: Although CO₂ fluxes constrained by atmospheric data in the Bayesian inversion framework inherit a dominant spatial

Deleted: Although CO₂ fluxes constrained by atmospheric data in date in the Bayesian inversion framework inherit a dominant ... [2]

Deleted: present

Deleted: to assess the impact of mesoscale transport on CO₂ estimates. In addition, the resulting impact from using differen... [3]

Deleted: on the flux estimates was

Deleted: D

Deleted: about

Deleted: -

Deleted: in this study are presented in the methods (Section 2).

Deleted: varying in regional and global transport models using the regional inversions CSR and LUMIA in Section 3. The results are

Deleted: carried out throughout this study

Deleted: atmospheric

Table 2). The default CSR inversion system utilizes pre-calculated footprints from the Stochastic Time-Inverted Lagrangian Transport model STILT (Lin et al., 2003) at the regional domain, and the TM3 model at the global scale, applying the two-step scheme inversion approach (Rödenbeck et al., 2009), to provide the far-field contributions to the regional domain. In the default setup of the inversion system LUMIA, the footprints are pre-calculated using the Lagrangian particle dispersion model FLEXPART (Pisso et al., 2019), and the far-field contributions are calculated using the global transport model TM5 in a separate global inversion run, applying the two-step scheme inversion as well. These default configurations in both systems constitute the base cases. We strive to restrict the differences in the inversion runs to the targeted components, i.e., regional transport, boundary conditions, and the inversion systems, so as to outline the impact of each suite. That is, input data such as measurements of CO₂ dry mole fraction and the a-priori fluxes, used as constraints based on Bayes inference, are identical for all runs. We exchangeably make use of the four combinations of transport model components, the regional and global models, in the two inversion systems. The impacts were evaluated using forward model runs to quantify the differences in CO₂ concentrations (simulated with prior fluxes) and inversion runs to quantify the magnitude of differences in the flux space. The inversion setups and implementation are explained in the protocol of comparison (Section 2.6).

Deleted: second

Deleted: the

2.1 Inversion Framework

In the following description we remind the reader about the basic principles of the inversion schemes. For detailed information about the mathematical schemes, the reader is referred to (Rödenbeck, 2005) for CSR and to Monteil and Scholze (2021) for LUMIA. Both systems rely on the Bayesian inference that accounts for observations and prior knowledge to regularise the solution of the ill-posed inverse problem where a unique solution does not exist due to the spatial scarcity of observations. Therefore, the optimal state vector (\mathbf{x}) is searched for in the Bayesian formalism by minimizing the cost function $J(\mathbf{x})$ that is typically composed of the observational constraint term $J_c(\mathbf{x})$ and the prior flux constraint term $J_b(\mathbf{x})$

$$J(\mathbf{x}) = J_c(\mathbf{x}) + J_b(\mathbf{x}) \quad (1)$$

where

$$J_b(\mathbf{x}) = \frac{1}{2} (\mathbf{x} - \mathbf{x}_b)^T \mathbf{B}^{-1} (\mathbf{x} - \mathbf{x}_b) \quad (2)$$

$$J_c(\mathbf{x}) = \frac{1}{2} (\mathbf{H}(\mathbf{x}) - \mathbf{y})^T \mathbf{Q}^{-1} (\mathbf{H}(\mathbf{x}) - \mathbf{y}) \quad (3)$$

The prior flux uncertainty defined in the covariance matrix \mathbf{B} limits the departure of the control vector (\mathbf{x}) to the prior flux vector (\mathbf{x}_b). Similarly, the observational constraint is weighted by the observational covariance matrix \mathbf{Q} that contains the so-called model-data mismatch error, including uncertainty of measurement, representativeness, and transport. This uncertainty is assigned to the diagonal of the matrix \mathbf{Q} for the respective sites based on the ability of the transport model to represent the atmospheric circulation at such locations. $\mathbf{H}(\mathbf{x})$ represents the atmospheric transport operator (i.e., calculated by STILT and FLEXPART in our inversions) that determines the relation between fluxes and the modeled tracer concentration, which corresponds spatially and temporally to a given vector of measurements \mathbf{y} . Following the gradient descent method, a

variational algorithm is applied iteratively to reach the best convergence (global minimum) of the cost function that satisfies
 290 the optimal solution of the control vector. The default configurations for constructing the covariance matrices of prior uncertainty are slightly different in CSR and LUMIA. Prior flux uncertainty is assumed to be around 0.47 PgC yr^{-1} over the full domain of Europe derived from the global uncertainty (2.80 PgC) assumed in the CarboScope global inversion for the annual biogenic fluxes (Rödenbeck et al., 2003). In CSR, this uncertainty is uniformly distributed spatially and temporally in a way that the annual uncertainty aggregated over the entire domain should arrive at the same value. The uncertainty
 295 structure is fit to a hyperbolic decay function in space (Eq. (4)) and to an exponential function (Eq. (5)) for the temporal decay as explained in Kountouris et al. (2015).

$$r(s) = \frac{1}{1 + \frac{s}{ds}} \quad (4)$$

$$r(t) = e^{-\frac{t}{dt}} \quad (5)$$

The correlation length scales ds and dt applied to flux uncertainties are chosen to be 66.4 km spatially and 30 days
 300 temporally, respectively, following Kountouris et al. (2018a) and Munassar et al. (2022). The spatial length in the zonal direction is set to be longer than that in the meridional direction by a factor of 2 (anisotropic), owing to larger spatial climate variability in meridional as compared to zonal direction.

The spatio-temporal shape of the prior uncertainty in LUMIA is computed in a way that each control vector comprises weekly uncertainty calculated as the standard deviation of NEE based on weekly flux variance; however, LUMIA agrees on
 305 the overall annually aggregated flux uncertainty over the entire domain with CSR. A Gaussian function of the spatial correlation decay (Eq. (6)) is applied to the prior uncertainty structure with a spatial length scale of 500 km

$$r(s) = e^{-\frac{s}{ds^2}} \quad (6)$$

whereas the effective temporal decay was set to 30 days (same as in CSR). Given the difference in the spatial correlation decay of the prior uncertainty, LUMIA is set to draw larger flux corrections in a broader radial area where stations exist
 310 following the gaussian decay with a longer length scale compared to the hyperbolic decay in CSR. In turn, the hyperbolic function has a larger impact in the further radial distances than the Gaussian function does, regardless of the longer spatial scale assumed with the Gaussian decay in a factor of around 7.5 in comparison with the hyperbolic decaying function.

2.2 Atmospheric transport models

Surface sensitivities are calculated using the STILT (Lin et al., 2003) and FLEXPART (Pisso et al., 2019) models at a
 315 horizontal resolution of 0.25-degree and hourly temporal resolution. Both models simulate the transport of air mass via releasing an ensemble of virtual particles at the locations of stations. The virtual particles are transported backward in time and driven by meteorological fields obtained from the European Centre for Medium-Range Weather Forecasts (ECMWF).
 STILT particles are transported 10 days backward in time and forced by forecasting data obtained from the high-resolution implementation of the Integrated Forecasting System (IFS HRES). For the FLEXPART model in standard operation,

Deleted: e

particles are followed for 15 days backward in time driven by ERA-5 reanalysis data. To keep the consistency with STILT footprints, the backward time of FLEXPART footprints was limited to 10 days in the inversions. After this backward time integration, the particles are assumed to leave the domain, even though a large number of particles are expected to escape after a few days. To better represent air sampling in the mixed layer, day-time observations are considered, except for 325 mountain stations where night-time observations are used instead (Geels et al., 2007). To ensure best mixing conditions, temporal windows were considered for simulating CO₂ dry model fractions over stations as explained in Section 2.4 (Table 1). In addition, release heights of particles are taken as the highest sampling level above ground at each measurement site. For high altitude receptors, such as mountains, a correction height is used in STILT in a way that the actual elevation of the station can be represented in the corresponding vertical model level (Munassar et al., 2022). In FLEXPART, the elevation 330 above sea level is taken as the model sampling height.

2.3 A priori and prescribed fluxes

Three components of prior and prescribed surface-to-atmosphere fluxes of CO₂ are obtained from 1) biogenic terrestrial fluxes, 2) ocean fluxes, and 3) anthropogenic emissions and kept identical in both systems. Prior net terrestrial CO₂ exchange fluxes, Net Ecosystem Exchange (NEE), are calculated using the diagnostic biogenic model Vegetation Photosynthesis and 335 Respiration Model (VPRM) (Mahadevan et al., 2008). VPRM calculates NEE at hourly temporal and 0.25-degree spatial resolution, and provides a partitioning of the net flux into gross ecosystem exchange (GEE) and ecosystem respiration. Data obtained from remote sensing provided through the MODIS instrument and meteorological parameters from ECMWF ~~drive~~ 340 both quantities of the light-dependent GEE and the light-independent ecosystem respiration. The model parameters were also optimised against eddy covariance data selected within the global FLUXNET site network across Europe in 2007 (Kountouris et al., 2015). For more details on the VPRM model, the reader is referred to Mahadevan et al. (2008).

Ocean fluxes are taken from Fletcher et al. (2007), which provide climatological fluxes at a spatial resolution of 5° x 4°, remapped to 0.25-degree to be compatible with the biosphere model fluxes. In addition, anthropogenic emissions are taken from the EDGAR_v4.3 inventory, and are updated to recent years according to British Petroleum (BP) statistics of fossil fuel consumption, and distributed spatially and temporally based on fuel type, category, and country specific emissions, using the 345 COFFEE approach (Steinbach et al., 2011). The emissions are remapped to a 0.25° spatial grid and to an hourly temporal resolution.

Biogenic terrestrial fluxes are optimized in the inversions, while the ocean fluxes and anthropogenic emissions are prescribed, given the better knowledge about their spatial and temporal distribution in comparison with the heterogeneity, variability, and uncertainty of the biogenic fluxes. Moreover, in the absence of observational constraints that help 350 discriminate the contributions from the three categories, we chose to prescribe the ocean fluxes and anthropogenic CO₂ emissions. This is also justified by the fact that the observation sites are located in areas where the biospheric flux influence is expected to dominate the variability of CO₂ concentration, but it means that errors in the fossil or ocean fluxes might be compensated by the inversions, and resulting in changes in the posterior NEE.

Deleted: derive

2.4 Observations

Measurements of CO₂ dry model fractions are collected through ICOS, NOAA, and pre-ICOS stations across the domain of Europe provided by Drought 2018 Team and ICOS Atmosphere Thematic Centre (doi:10.18160/ERE9-9D85, 2020). In total, datasets from 44 stations are used covering the domain of Europe in 2018, in which a maximum number of stations is present compared to the other years. Regarding model-mismatch errors, in LUMIA a weekly value of 1.5 ppm is assumed to all sites
 360 except for the Heidelberg site where 4 ppm was assumed due to the anthropogenic influence from the neighbourhood. Table 1 denotes the weekly values of uncertainty used in CSR for the corresponding sites. The uncertainty for the surface sites is inflated to 2.5 ppm as a slight difference to LUMIA. The inflation of uncertainty from weekly to hourly values is basically calculated by multiplying weekly errors by $\sqrt{7 \times n}$ (n refers to the number of hours in the daily measurements used in the inversion). The observations are mostly assimilated as hourly continuous measurements, and are taken from the highest
 365 level, avoiding large vertical gradients near the surface that are hard to represent in the transport models. Model error in representing observations in the PBL is expected to be largest when the PBL is shallow. Therefore, for most sites, we considered data only when the PBL was expected to be well developed, i.e., during the afternoon, local time (LT). The exception is at high altitude sites, which tend to sample the free troposphere during night (Kountouris et al., 2018b). The assimilated windows are reported in Table 1.

2.5 Boundary conditions

Far-field contributions of CO₂ concentrations (originating from sources outside of the regional domain) are taken from global inversions. As default setups of the global runs, the Eulerian transport model TM3 is used in the CarboScope global inversion at 5° (lon) x 4° (lat), while TM5-4DVAR (Transport Model 5 – Four Dimensional Variational model) is used to
 375 provide boundary conditions to LUMIA using the global transport model TM5 at 6° (lon) x 4° (lat) (Babenhauserheide et al., 2015; Monteil and Scholze, 2021). Both inversion systems apply the two-step scheme inversion, explained in Roedenbeck et al. (2009), in which a global inversion is first used to estimate CO₂ fluxes globally (based on observations inside and outside Europe). In a second step, the global transport model is used to estimate the influence of European CO₂ fluxes on European CO₂ observations. That regional influence is then subtracted from the total concentration, to obtain a time-series of the far-field influence directly at the locations of the observation sites. This prevents introducing biases by passing concentration
 380 fields from one model to another. For detailed information about the approach methodology, the reader is referred to Roedenbeck et al. (2009).

2.6 Comparison protocol

The results of the study are based on eight variants of inversions differing in global and regional transport models, as well as in inversion systems as explained in Table 2. This implies, the two inversion systems (CSR and LUMIA) make use of two
 385 regional transport models (STILT and FLEXPART) and two global transport models (TM3 and TM5), which represent the

Deleted: (Babenhauserheide et al., 2015)

Deleted: in

Deleted: (Monteil and Scholze, 2021)

boundary conditions (background) calculated from two global inversions. Hereafter, the identifier codes (see corresponding 390 column in Table 2) will be used to refer to the individual runs within the inversion ensemble. For instance, to highlight the impact of regional transport models, we compare the inversions that only differ in regional transport models, regardless of the inversion system or boundary conditions used, such as CS3 and CF3 or LS5 and LF5. Similarly, we use the same specifications of transport models (indicated through the identifier codes) for the forward runs to outline the differences in CO₂ concentrations simulated using prior fluxes with different transport models. In this case using a different system should 395 not result in discrepancies as long as prior fluxes remain identical. In terms of system-to-system comparison, the impact of flux uncertainty should be taken into account as the prior error structure is specific for each inversion system. With that said, this has been investigated by conducting additional tests in CSR and LUMIA using identical uncertainties with flat shape and Gaussian correlation decay.

Deleted: However

3 Results

400 Estimates of the regional biosphere-atmosphere fluxes over the domain of Europe are calculated using CSR and LUMIA for 2018 from an ensemble of eight inversions as listed in Table 2. Generally, all the inversions showed that the estimates of NEE are constrained by the atmospheric data as can be seen from the positive flux corrections made by the inversions in comparison with the prior fluxes calculated from the biosphere flux model VPRM, which obviously overestimates CO₂ uptake, specifically during the growing season (Fig. 1, left). This is also obvious in the ensemble-averaged annual estimates 405 of posterior fluxes -0.29 PgC versus -1.49 PgC in the prior fluxes (Fig. 1, right). However, the spread among posterior estimates is still relatively large ranging between -0.72 and 0.20 PgC yr⁻¹ for the annual estimates, larger than the prior uncertainty of 0.47 PgC yr⁻¹. Likewise, the mean standard deviations of the monthly estimates over the ensemble of inversions is 0.72 (PgC yr⁻¹). The largest deviations occur between inversions that differ by the regional transport models (e.g., CS3 versus CF3, or LS5 versus LF5). In addition, the seasonal amplitude was found to be different between the STILT, 410 and FLEXPART, inversions. The STILT-based inversions lead to a larger amplitude of posterior NEE than the FLEXPART-based inversions.

Deleted: <#>Main inversion results

We present eEstimates of the regional biosphere-atmosphere t... [4]

Deleted: The mean of ...standard deviations of calculated for ... [5]
Formatted: Superscript

415 In terms of spatial distributions, the base cases of CSR and LUMIA inversions, i.e., CS3 and LF5 (default configurations of both systems), exhibit good agreement in predicting smaller uptake of CO₂ compared to the a-priori fluxes (Fig. 2, first row). The magnitude of flux corrections suggest more additional sources inferred from the atmospheric signal, as shown in the innovations of fluxes (Fig. 2, second row). Major corrections are obtained over western and southern Europe where the inversions point to an overestimation of the CO₂ uptake by the prior biogenic fluxes. The weak annual uptake of CO₂ in 2018 was exceptional and caused by the drought episode in Europe (Bastos et al., 2020; Rödenbeck et al., 2020; Thompson et al., 2020), which even turned some areas in central, northern, and western Europe into a net source of CO₂. The discrepancies between CS3 and LF3 noticed in the innovations, e.g., in northern France, Netherlands, and south-eastern UK are 420 attributable to the combination of differences in regional transport models, lateral boundaries, and system configurations.

Deleted: t

The ...patial distributions, of NEE is illustrated in Fig. 2 (first ... [6]

Deleted: Posterior NEE suggests aThe weaker...annual ann... [7]
Formatted: Subscript

Formatted: Subscript

Deleted: t

... [8]

In the following we will focus on separating and quantifying the contributions of such differences caused by each driver.

495 3.1 Impact of mesoscale transport

Inversions that differ in the regional transport models (STILT and FLEXPART) demonstrate the largest differences in posterior fluxes resulting in a relative contribution of about 61% of the total differences compared to the boundary conditions and inversion systems. The differences in monthly estimates of NEE calculated with CS3 and CF3 inversion setups that vary in regional transport models are shown in Fig. 3 (top panel, "transport"). Additionally, the discrepancies caused by transport 500 have an obvious seasonal pattern. The differences between CS3 and CF3 peak in November and June, reaching 2.11 and -1.82 (PgC yr⁻¹), respectively. The best agreement between both inversions is obtained during the transitional months (August and April) with differences of -0.10 and -0.18 (PgC yr⁻¹), respectively. This might be attributed to the decline of the net flux magnitude during these months.

Furthermore, we assessed the impact of atmospheric transport in the simulations of CO₂ concentrations because this directly 505 translates into differences in the optimised fluxes. These simulations were calculated using the total components of prior fluxes (biosphere, ocean, and fossil fuel emissions) with STILT and FLEXPART in forward model runs to sample the atmospheric concentrations at hourly time-steps at the station locations across the site network. Note that since all runs use identical prior fluxes, it does not matter for the differences whether the prior fluxes were precise enough to reproduce the true concentration or not. Figure 3 (bottom panel, "transport") illustrates the monthly differences in the forward simulations 510 between STILT and FLEXPART averaged over all observational stations. Similarly to the discrepancies in the optimised fluxes, the differences in the forward simulations demonstrate a dominant impact of the regional transport model preserving the same temporal pattern as seen in the flux differences but with opposite signs. The absolute difference ranges from 0.39 to 4.37 (ppm) computed for the monthly means throughout all the sites. Geels et al. (2007) found even a larger spread up to 10 (ppm) calculated with five transport models over ten stations distributed across Europe. The notably large difference 515 reported in that study is likely attributed to the large discrepancies in the model configurations, especially regarding the horizontal resolution and vertical levels used. The harmonised configurations used in STILT and FLEXPART lead to a reasonably consistent representation of the atmospheric variability at synoptic and diurnal timescales. The largest differences are observed during November and May with -4.37 and 3.60 (ppm), respectively. On the other hand, the smallest differences were found to be -0.39, -0.42, and 0.56 (ppm) during September, April, and August, respectively. These results suggest a 520 maximum impact of the mesoscale transport during the growing season and winter, while the impact converges to the minimum during transitional months such as May and September. Overall, the differences in posterior fluxes are consistent in the timing with the differences in the simulated concentrations computed using the prior fluxes.

Deleted: sections

Deleted: attempt

Deleted: to

Deleted: e

Deleted: - i.e., mesoscale transport, lateral boundaries, and system configurations.

Differences in optimized fluxes and forward simulations¹. In this section, we look at the impact of changing individual components of the inversion system on the inversion results, and we put them in relation to differences in prior model-data mismatches. Differences in the optimized monthly fluxes caused by the different regional transport models, different inversion systems, and different boundary conditions are shown in Fig. 3 (top). Inversions differing in the regional transport models STILT and FLEXPART exhibit the largest differences in posterior fluxes (transport). The discrepancies caused by transport indicate an obvious seasonal pattern, while boundary conditions (background) and inversion systems (system) appear to result in smaller differences that are systematic across all months for the background and more random for the differences related to inversion systems. The magnitude of flux differences is found to be larger in the background compared to inversion systems. Figure 3, bottom, illustrates the magnitude of differences in forward simulations of CO₂ concentrations at hourly time-steps, computed using prior fluxes, averaged over the observational sites distri... [9]

Moved down [2]: In this case, the forward model runs with

Deleted: Differences in optimized fluxes and forward sim... [10]

Formatted: Line spacing: Multiple 1,63 li

Moved (insertion) [1]

Deleted: STILT-

Deleted: FLEXPART-based

Deleted: inversion results for the monthly domain-aggrega... [11]

Deleted: ed

Deleted: yielding

Deleted: realized

Deleted: pointing to

Deleted: can

Deleted:

Moved (insertion) [5]

Deleted: Forward runs conducted with STILT and FLEXP... [12]

Deleted: S

Deleted: utilize

Moved (insertion) [2]

Deleted: In this case

Deleted: the forward model runs

Deleted: with STILT and FLEXPART using TM3 bounda... [13]

Deleted: quite

Deleted: large differences

Further diagnostics of model-data mismatches are provided in the supplementary materials indicating the performances of 645 STILT and FLEXPART with respect to the observations using prior and posterior fluxes across the site network at hourly, weekly and yearly time steps (see Fig. 1S and Table 1S).

In terms of the spatial discrepancies in annual flux estimates, using STILT generally leads to predicting a larger sources of 650 CO₂ in the regional inversions, in particular over central Europe and the UK compared to using FLEXPART (Fig. 4, "diff: transport"). In turn, inversions using FLEXPART suggest less uptake over northern Italy, Switzerland, and south-eastern France. However, this impact refers to a spatial pattern of transport differences that might be caused either by meteorological data or by problematic sites that are hard to represent by transport models. Some areas such as north-western Italy exhibit a persistent impact over time as shown in Fig. 4 ("sd: transport"), which shows the standard deviation of monthly differences calculated for the CS3 and CF3 inversions. In terms of temporal variations, the inversions performed with different regional transport models indicate larger monthly flux variations in comparison with those differing in global models and inversion 655 systems (see Fig. 4, "sd: background" and "sd: system").

Figure 5 shows the spatial flux differences together with differences in prior concentrations simulated using STILT and FLEXPART during June and December. Noteworthy, the differences in NEE, to a large extent, agree in their spatial patterns with the differences in prior concentrations calculated over the station network. In addition, there are notably particular areas that exhibit opposite signs of the spatial impact in the differences in posterior fluxes and prior concentrations such as western 660 Europe during June and northern Europe during December. One important difference between STILT and FLEXPART is that the STILT model has higher sensitivities during summer than FLEXPART, while the opposite holds true during winter. However, there are exceptions at individual sites such as Weybourne (WAO) in the UK and Ispra (IPR) in Italy indicating either difficult terrains that cannot be well represented by the models or real synoptic features that are resolved by one model but not by the other. The differences in forward simulations are inversely manifested in the posterior flux differences as large 665 surface sensitivities result in smaller posterior flux corrections, and vice versa. In this case, STILT computes higher surface sensitivities than FLEXPART in June; therefore, the CS3 inversion needs to adjust less the prior fluxes to fit the observations. On the contrary, a weaker uptake is suggested by STILT inversion during December over Europe, except for the abovementioned areas around northern Italy and south-eastern France. The differences appeared to be larger during the months of growing season and winter following the seasonal amplitude of CO₂.

670 3.2 Impact of lateral boundary conditions

The differences in lateral boundary conditions were found to account for about 27% of the total differences resulting from the regional transport, lateral boundaries, and systems. This is a non-negligible contribution, albeit smaller than the regional transport contribution. The impact of using different far field contributions was analysed by assessing the differences in the posterior NEE estimated with CS3 and CS5 inversions, which use boundary conditions from the global inversions

Deleted: In this section, we use the inversion results obtained from CS3 and CF3 to analyse the differences in flux estimates resulting from varying regional transport models. ...

Deleted: The regional transport leads to large spatial

Deleted: (Fig. 4, "diff: transport")

Deleted: .

Deleted: U

Deleted: release

Deleted: Unlike other

Deleted: , this impact is

Deleted: months

Deleted: ,

Deleted: shown

Deleted: by

Deleted: which

Deleted: between

Deleted: the context of

Moved up [1]: The differences between STILT- and FLEXPART-based inversion results for the monthly domain-aggregated estimates (Fig. 3, top) peaked in November and June yielding 2.11 and -1.82 (PgC yr⁻¹), respectively. The best agreement between both inversions is realized during the transitional months (August and April) pointing to differences of -0.10 and -0.18 (PgC yr⁻¹), respectively. This can be attributed to the decline of the net flux magnitude during these months. Regarding differences in the forward simulations (Fig. 3,

Deleted: The differences between STILT- and FLEXPART-based inversion results for the monthly domain-aggregated estimates (Fig. 3, top) peaked in November and June yielding 2.11 and -1.82 (PgC yr⁻¹), respectively. The best agreement between both inversions is realized during the transitional months (August and April) pointing to differences of -0.10 and -0.18 (PgC yr⁻¹), respectively. This can be attributed to the decline of the net flux magnitude during these months. Regarding differences in the forward simulations (F^{...} [14]

Deleted: . The prior concentrations were calculated at hourly time steps at the observational sites based on prior fluxes...

Deleted: Positive differences in simulated prior concentrations correspond to negative differences in optimized fluxes due to the fact that greater surface sensitivities will result in small flux corrections in the flux space, and vice versa. In this case, STILT computes higher surface sensitivities than FLEXPART in June, therefore the CS3 inversion needs to adjust less the prior fluxes to compensate for this. On the contrary, a weaker uptake is suggested by STILT inversion during December over Europe compared to the FLEXPART ... [15]

Deleted: in which the differences in posterior fluxes and p ... [16]

Deleted: To highlight

Deleted: t

Deleted: arising from

Deleted: on the estimates of regional NEE

735 CarboScope and TM5-4DVAR, respectively. Figure 3 (“background”) shows consistent differences over time between these inversion estimates aggregated over the entire domain of Europe. Larger flux corrections are suggested by CS5 than by CS3. This is because the global TM3-based inversion predicts higher influence at the lateral boundaries than the global TM5-based inversion does. Discrepancies in the monthly posterior fluxes between CS3 and CS5 inversions amount to a range of 0.11 to 0.64 (PgC yr⁻¹) absolute differences with a mean of 0.40 (PgC yr⁻¹). Monthly mean differences in CO₂ concentrations throughout all sites simulated using TM3 and TM5 boundary conditions were found to range from 0.17 to 0.93 (ppm) with a mean of 0.55 (ppm).

740 The distributions of spatial differences of posterior fluxes indicate a homogeneous impact across the full domain of Europe (Fig. 4, “diff: background”). Likewise, the standard deviations of the monthly posterior fluxes obtained from CS3-CS5 (“sd: background”) denote flat temporal variations throughout all the grid-cells. These findings confirm the results obtained in Fig. 745 3 “background”. This impact is consistent in space and time, with coherent deviation over all months, and is therefore expected to not affect the seasonal and interannual variability.

3.3 Impact of inversion systems

750 CS3 and LS5 differ by more than their regional transport and boundary conditions. In particular, the uncertainties are, by default, setup differently in CSR and LUMIA. The two systems optimise different set of variables (weekly NEE offsets in LUMIA and 3-hourly NEE in CSR). Here we compare CS5 and LS5, which differ by their inversion systems but not by their transport model and boundary conditions. The differences in flux estimates between CS5 and LS5 inversions amount to 12% relative to the total differences, including that caused by the mesoscale transport and lateral boundaries. This impact is, however, dependent upon system configurations, in particular the way how the prior flux uncertainty is prescribed. The absolute monthly differences between CS5 and LS5 range between 0.06 and 0.56 (PgC yr⁻¹) with a mean of 0.15 (PgC yr⁻¹) (Fig. 3, “system”). This demonstrates the smallest differences amid inversions in comparison with the transport and lateral boundary differences, which yielded absolute monthly means of 1.27 and 0.40 (PgC yr⁻¹), respectively. The differences peaked during May, June, and November, while the differences remained rather small during the rest of the year. LS5 infers -6.42 and 2.39 (PgC yr⁻¹) during June and December, respectively, which is higher than CS5 estimates by 0.33 and 0.07 (PgC yr⁻¹). Generally, LS5 predicts slightly larger CO₂ releases compared to CS5, which is partially due to differences in how uncertainties are assumed in both systems.

760 The impact of uncertainty definition is quantitatively assessed through using identical uncertainties for model-data-mismatch as well as for prior fluxes in both CSR and LUMIA. The spatial flux corrections (innovation of fluxes) shown in Fig. 8 denote quite good agreement between CSR and LUMIA estimates. In this experiment, the differences in June and December decreased to 0.23 and 0.04 PgC yr⁻¹, respectively, in comparison with the corresponding differences obtained from the 765 default configurations of both systems. That is to say, the impact of uncertainty definition alone amounts to 0.09 and 0.03

Deleted: , Figure...34... (“diff: ...background”) shows the ... [17]

Moved (insertion) [3]

Deleted: It can be seen from this impact that l...arger flux ... [18]

Formatted: Subscript

Deleted: that differ in the global transport models (TM3 versus TM5). The

Deleted: contributions of lateral concentration appear to... ... [19]

Formatted: Line spacing: Multiple 1,63 li

Moved (insertion) [4]

Deleted: Unlike the regional transport model impact, the boundary condition impact does not lead to seasonality in the differences of CO₂ concentrations (Fig 3, bottom), in alignment with the differences in fluxes (Fig. 3, top). The differences are also much smaller than those resulting from swapping the regional transport models, with monthly mean differences ranging from 0.17 to 0.93 (ppm), with a mean of 0.55 (ppm). That way the posterior contribution of regional fluxes to CO₂ concentrations increases to compensate for the lower far-field influence. This is mostly the case for stations located inside the regional domain apart from boundaries. [4]

Moved up [3]: It can be seen from this impact that larger flux corrections are suggested with the TM5-based inversion compared to TM3-based inversion. Discrepancies in the monthly posterior fluxes between CS3 and CS5 inversions amount to a range of 0.11 and 0.64 (PgC yr⁻¹) absolute differences with a mean of 0.40 (PgC yr⁻¹). These differences are obviously smaller than the differences in the mesoscale transport inversions but notably larger than the differences arising when replacing the inversion system. [4] ... [20]

Deleted: From the perspective of temporal differences, using different lateral boundaries shows a smaller impact on optimized fluxes aggregated over the entire domain of Europe compared to the mesoscale transport impact as illustrated in the difference between the two inversions CS3 and CS5 (Fig. 3). It can be seen from this impact that larger flux corrections are suggested with the TM5-based inversion compared to TM3-based inversion. Discrepancies in the monthly posterior fluxes between CS3 and CS5 inversions amount to a range of 0.11 and 0.64 (PgC yr⁻¹) absolute differences with a mean of 0.40 (PgC yr⁻¹). These differences are obviously smaller than the differences in the mesoscale transport inversions but notably larger than the differences arising when replacing the inversion system. [4]

Deleted: inversion systems between CS5 and LS5 invasio... ... [21]

Moved (insertion) [6]

Deleted: Using a different inversion system results in non-negligible differences in CO₂ flux estimates, albeit smaller than that resulting from transport and lateral boundaries. This impact is however dependent upon system configurations, in particular the way how the flux uncertainty is prescribed. For example, LS3 predicts -6.416 and 2.387 (PgC yr⁻¹) during June and December, respectively, which is higher than CS3 estimates by 0.325 and 0.067 (PgC yr⁻¹). Generally, LUMIA predicts slightly larger CO₂ releases compared to CSR, which is partially attributed to differences in uncertainties assumed in both systems. ...

Deleted: through through utilizing...ing identical uncertain... ... [22]

Formatted: Line spacing: Multiple 1,63 li

905 PgC yr⁻¹ in June and December, respectively, leading to approximately 30% and 50% of the overall system-to-system differences. The rest of the differences may be attributed to differences in the convergence of the cost function to reach the minimum values.

The spatial differences shown in Fig. 4 (“diff: system”) alter between positive and negative differences over the domain (but these tend to compensate when aggregating the flux estimates over the full domain). It should be noted that the inversion 910 systems mainly differ in the definition of the shape and structure of the prior uncertainty. Therefore, applying different structure and magnitude of prior flux uncertainty in the inversions may inflate the error in CO₂ flux estimates over the underlying regions in the domain, in particular if the spatial differences do not cancel out. In addition, the corresponding standard deviations of monthly estimates (“sd: system”) show large temporal variations, specifically over areas that have 915 large spatial differences. The spatial results indicate that the impact of inversion systems should not be neglected, especially at national and subnational scales.

4 Discussion

The regional inversions computed over Europe showed that posterior NEE is largely derived from the atmospheric signal. The seasonality of posterior NEE, inferred from the atmospheric signal, is strongly impacted by differences in the 920 representation of atmospheric transport. Given the identical priors and observational datasets used in the inversions, using different mesoscale transport models leads to 61% of the differences in posterior fluxes in comparison with 27% and 12% of the differences caused by the use of different boundary conditions and different inversion systems, respectively. In agreement with these results, Schuh et al. (2019) also found a large impact of mesoscale transport on estimating CO₂ fluxes. Hence, any error in the atmospheric transport is translated into posterior fluxes as flux corrections. For instance, CS3 and LS3 suggest annual CO₂ flux budgets of -0.20 and -0.72 PgC, respectively, indicating a difference of 0.51 PgC in the annual 925 flux budget. This difference is even larger than the prior flux uncertainty (0.47 PgC). The transport also showed a large impact on flux seasonality leading to a difference of 49% relative to the mean seasonal cycle. However, Schuh et al. (2019) found smaller differences amounting to about 10-15% of the mean seasonal cycle. Unlike the regional transport model error, the impact of boundary conditions does not show any striking seasonality and thus can be thought of as a bias in dry mole 930 fractions. The consistency of the lateral boundary impact over time and space is in agreement with results of lateral boundary uncertainties assessed by Chen et al. (2019) using four different global transport models, albeit over a different domain. Therefore, such an impact may be dealt with as a constant correction in mixing ratios before performing the regional inversions, potentially site-specific corrections. But there should be a reference for these corrections, for example, taking the most robust model that has been validated against observations or simply a factor of the relative mean of the relevant models/approaches. Although the inversion systems showed the smallest differences in CO₂ flux estimates, the specification

Deleted: t

Formatted

Deleted: (

Deleted:)

Deleted: in particular

Deleted: indicate

Deleted: a non-negligible

Deleted: impact of inversion systems

Deleted: The inversions generally predict weaker

Deleted: annual uptake of NEE over the entire domain of Europe than does the prior biosphere flux model. Seasonality of ...

Deleted: ;

Deleted: however,

Deleted: t

Deleted: seasonal amplitude demonstrates large differences due mainly to the transport ...

Deleted: leads

Deleted: .

Deleted: H

Deleted: R

Deleted: inversions

Deleted: an

Deleted: PgC with STILT

Deleted:

Deleted: with FLEXPART

Deleted: A better illustration of NEE differences can be obtained when comparing June and December estimates among the different inversions, so as to avoid the compensating effect of CO₂ seasonality. The differences arising from the mesoscale transport during June and December were found to be -1.82 and 1.75 PgC yr⁻¹, respectively (see Fig. 3). This finding is in agreement with Schuh et al. (2019) indicating the large impact of mesoscale transport on estimating CO₂ fluxes. The transport also showed a large impact on flux seasonality leading to a difference of 49% relative to the mean seasonal cycle. However, Schuh et al. (2019) found smaller differences amounting to about 10-15% of the mean seasonal cycle. In a relevant study, Deng et al. (2017) estimated CO₂ emissions using four different setups of meteorological data assimilations in the transport model and found a difference of about 15% in the local corrections although the error reduction of wind direction and wind speed was about 50% due to data assimilation, while the difference over the entire domain was confined to less than 5%. These results finding refer to the limited impact of meteorological data. Unlike the regional transport model

of the control vector (regarding the construction of covariance matrices) that devises the flux correction can result in larger differences, specifically in the spatial flux patterns.

The large number of stations within central and western Europe lead to a strong observational constraint that is reflected in

980 the spatial optimized fluxes over that area. Therefore, large spatial differences between the inversions are pronounced around areas where stations exist, precisely for grid cells that have non-zero footprints. The large temporal variations indicate a systematic error that possibly arises from the transport models themselves as well as from meteorological forcing data. Additionally, systematic differences between transport models occur due to discrepancies in representing vertical mixing and horizontal and vertical resolution of the models (Peylin et al., 2002). Gerbig et al. (2008) found large discrepancies in 985 derived mixing heights between meteorological analysis from ECMWF and radiosonde data, which reached about 40% for the daytime and about 100% for the nocturnal boundary layer. The vertical mixing in tracer dispersion models was found to result in a significant variability in methane emission estimations (up to a factor of 3) given the same meteorology as investigated by Karion et al. (2019).

Deleted: A stronger flux gradient in the meridional direction is noticed in posterior flux maps of CSR compared to the zonal direction due to the anisotropic spatial correlation length of prior error structure. The large temporal variations indicate a systematic error that possibly arises from the transport models themselves as well as from meteorological forcing data. Additionally, systematic differences between transport models occur due to discrepancies in representing vertical mixing and horizontal and vertical resolution of the models (Peylin et al., 2002). Gerbig et al. (2008) found large discrepancies in derived mixing heights between meteorological analysis from ECMWF and radiosonde data, which reached about 40% for the daytime and about 100% for the nocturnal boundary layer. The vertical mixing in tracer dispersion models was found to result in a significant variability in methane emission estimations (up to a factor of 3) given the same meteorology as investigated by Karion et al. (2019).

Deleted: , as will be discussed

990 Drivers of STILT-FLEXPART differences

Although STILT and FLEXPART are run at the same spatio-temporal resolution employing similar schemes to parametrize the atmospheric motion unresolved by meteorological forcing data such as turbulence, and similar diagnostics to determine mixing heights, they still exhibit large spatial and temporal differences. A first assumption was that the differences between STILT and FLEXPART could be caused by differences in the calculation of mixing height. However, we did not find a 995 correlation between the differences in mixing heights, calculated with the two models, and the differences in prior concentrations (Fig. 6). This finding concludes that the discrepancies in representing mixed layer heights do not explain the major differences in simulated CO₂ concentrations nor the differences in footprints.

The second assumption was that differences in the forcing data of meteorological products might lead to the discrepancies in both models, given that STILT uses meteorological parameters from IFS HRES, while FLEXPART uses ERA-5 reanalysis.

1000 Results in Fig. 7, "meteo", indicate that using different meteorological data results in pronounced differences when the FLEXPART model was forced by operational forecast data instead of ERA-5 reanalysis. These differences notably occur during the time of net CO₂ release corresponding to quite small differences during the time of growing season. This, however, only explains a small part of the overall differences (shown in Fig. 7, "base") that dominate all the months except August and September. In a previous study, Liu et al. (2011) concluded that uncertainties in meteorological fields lead to a 1005 significant contribution to the total transport error, as well as to an underestimation of the vertical turbulent mixing even when the same circulation model and mixing parameterizations were used to reconstruct vertical mixing from a single meteorological analysis. Tolk et al. (2008) also found meteorology to be a key driver of representation error, which varies spatially and temporally. They indicated that a large contribution to representation error is caused by unresolved model

Moved up [5]: Forward runs conducted with STILT and FLEXPART to sample CO₂ concentrations over the station network point out the spatial difference between the models in simulating the concentration at the locations of sites (Fig. 5). Since all runs utilize identical prior fluxes, it does not matter for the differences whether the prior fluxes were precise enough to reproduce the true concentration or not. The monthly

Deleted: Forward runs conducted with STILT and FLEXPART to FLEXPART to sample CO₂ concentrations over the station network point out the spatial difference between the models in simulating the concentration at the locations of sites (Fig. 5). Since all runs utilize identical prior fluxes, it does not matter for the differences whether the prior fluxes were precise enough to reproduce the true concentration or not. The monthly average differences over a ... [23]

Deleted: Due to the fact that deep mixed layer heights dilute the tracer concentration owing to the radiative heating process taking place during day-time, the surface sensitivity and atmospheric stratification are expected to decrease accordingly. Thus, a logical assumption is that large values of STILT footprints during the growing season, as supported by the simulations of forward model runs, would probably be caused by a shallower mixing height in comparison with FLEXPART footprints, while FLEXPART footprints demonstrate larger values during winter for the same reason. However, the relationship between the differences of prior concentrations and the differences of mixed layer heights computed with the two models do not show a striking correlation, as can be seen from the scatter plots of the differences in Fig. 6. This finding

Deleted: the

Deleted: simulations

Deleted: y

topography at coarse spatial resolution during night, while convective structures, mesoscale circulations, and the variability of CO₂ fluxes dominate during day-time. Deng et al. (2017) found that assimilating meteorological observations such as wind speed and wind direction in transport models significantly improved the model performances achieving an uncertainty reduction of about 50% in wind speed and direction, especially when measurements in the mixed layer were assimilated. Nonetheless, they concluded that the differences in CO₂ emissions reached up to 15% at local scale corrections after inversion and were limited to 5% for the total emissions integrated across the regional domain of interest. These results refer 045 to the limited impact of meteorological data. Note however that the main aim of this experiment was to test whether differences in driving meteorological data could explain the differences between STILT and FLEXPART, but that we are not assessing the overall impact of meteorological uncertainties. Doing so would in particular require testing non-ECMWF meteorological products.

Furthermore, we tested the possible impact of surface layer heights (the height up to which particles are sensitive to the fluxes) that may affect the particle dispersion, provided that STILT relies on the assumption of defining the surface layer as a half of the mixed layer height, while in FLEXPART it is defined as a fixed height of 100 m (these are default configurations of the models). In this experiment, STILT was run with a surface layer height of 100 m, so that the impact of the surface layer on CO₂ simulations is outlined by the comparison with another run using the default configurations of STILT. The differences in simulated CO₂ concentrations due to differences in the surface layer were found to be quite small (Fig. 7, 050 "s_layer") and, therefore, can be negligible in both magnitude and temporal pattern compared to the overall differences. However, varying the models STILT and FLEXPART with identical meteorological data and identical surface layer lead to the largest differences, in particular during the growing season months and winter months (Fig. 7, "model"). As a result, 055 model-to-model differences largely affect the simulations of CO₂ concentrations and are likely originating from the transport model schemes. It is clearly noticeable that the overall differences combine the underlying differences of "model", "meteo", and "s_layer", and are yielded as the arithmetic summation of this partitioning.

How do our results explain the range of uncertainties reported in scientific literature?

To shed more light on the drivers of differences in optimised CO₂ fluxes, we analyse the spread in our inversions in line with the spreads in other inversion estimates that were reported in two previous studies over the same domain of Europe. Figure 9 shows the spreads amid the three studies: 1) eight inversions conducted in our results denoted as "Ensemble", 2) six 060 inversions of the EUROCOM experiment "EUROCOM" done by Monteil et al. (2020), and 3) five inversions of the drought study of Thompson et al. (2020) focusing on analysing the 2018 drought impact on NEE, denoted as "Drought". Note that in EUROCOM and Drought, the tracer inversions differed in the atmospheric regional transport models, the definition of boundary conditions, the definition of control vector, the selection of atmospheric datasets, and the a-priori fluxes. These differences are expected to span a large range of uncertainty sources in the posterior NEE. The climatological monthly 065

Deleted: In our analysis, one should take into consideration that both operational forecasts and ERA-5 are ECMWF products and thus are expected not to significantly diverge. ...

Deleted: When running STILT with a surface layer of 100 m,

Deleted: :

Deleted: with the default STILT run

Deleted: (Fig. 7, "s_layer")

Deleted: (

Deleted: are driven by IFS data and using a surface layer of 100 m)

Deleted:

Deleted: as seen from

Deleted: (

Deleted: parameterizations

Deleted: are expected to be the main driver of differences

Deleted: (default configurations of the models)

Deleted: Therefore, the differences in CO₂ simulations should considerably be dealt with as a model-model error. A further study would be needed to investigate the main drivers of these discrepancies in both STILT and FLEXPART for further model developments.¶

Impact of lateral boundaries and systems¶

In terms of far field contribution impact, smaller differences of CO₂ estimates are observed when varying the global transport models compared to the mesoscale transport. The differences in posterior fluxes arising from boundary conditions amount to 0.40 (PgC yr⁻¹) during June and 0.11 (PgC yr⁻¹) during December. This impact was found to be consistent in space and time, with coherent deviation over months, and is not therefore expected to affect the seasonal and interannual variability. Unlike the regional transport model error, this kind of error can be thought of as a bias in dry mole fractions, which may be dealt with in the inversions as a constant correction, potentially site-specific correction. The differences between far field contributions suggest that using TM3 leads to smaller regional signal of mole fractions used to constrain fluxes in comparison with TM5. The consistency of the lateral boundary impact over time and space is in agreement with results of lateral boundary uncertainties assessed in Chen et al. (2019) using four different global transport models, albeit over a different domain.¶

Moved up [6]: Using a different inversion system results in non-

Deleted: Impact of lateral boundaries and systems¶ ... [24]

Deleted: We attempt here

Deleted: :

Formatted: Subscript

Deleted: calculated over different ensembles of

Deleted: inversions reported in previous studies by Monteil et al. (2020) in the EUROCOM experiment and by Thompson et al. ... [25]

Deleted: ensembles

Deleted: of

Deleted: Thompson et al. (2020)

estimates of NEE were averaged over “EUROCOM” inversion members for the respective years 2006-2015, except for one inversion (NAME), which was limited to 2011-2015. “Ensemble” and “Drought” were confined to the analysis year of 2018.

1170 The monthly NEE estimates were calculated for all ensembles as the average over their respective inversion members. The annual mean of NEE estimated with “EUROCOM”, “Ensemble”, and “Drought” amounts to -0.19 and -0.29, and -0.05 (PgC) with standard deviations of 0.34 and 0.29, and 0.46 (PgC), respectively.

The spreads amid each ensemble of inversions are illustrated by the min and max values bounded around the mean on the error bars (Fig. 9). The monthly mean of NEE estimates shows a good consistency in all the ensembles. The spreads are also 1175 relatively comparable, albeit variable over months. For instance, “EUROCOM” and “Drought” exhibit larger spreads during the growing season (April-August), while “Ensemble” has a larger spread in the rest of months -i.e., during winter. Noteworthy, all ensembles experience large spreads during June and May. Although the participating inversions to “EUROCOM” and “Drought” had different configurations, the spreads were not largely different from our inversion spreads. This implies that the use of different atmospheric transport models could account for a large fraction of differences in 180 posterior fluxes, although differences in the definition of uncertainty covariance matrices and lateral boundary conditions likely contribute as well. Moreover, the discrepancies in “EUROCOM” and “Drought” estimates are expected to be partially caused by using different atmospheric datasets in the inversion systems. Munassar et al. (2022) found that posterior fluxes can be more sensitive to changing the number of stations than changing the prior flux models.

5 Conclusions

1185 Estimating atmospheric tracer fluxes through inverse modeling systems has been widely used, in particular targeting the major GHGs to improve the quantification of natural (both terrestrial and oceanic) sources and sinks. Here, an analysis of differences in posterior fluxes of CO₂ was carried out using inversion systems deploying different regional transport models. The difference between minimum and maximum spreads for annually integrated fluxes was found to be 0.92 PgC yr⁻¹ for the ensemble range of 0.20 and -0.72 PgC yr⁻¹ with a mean estimate of -0.29 PgC yr⁻¹ calculated over the full domain of Europe 190 in 2018. We tested the regional transport, the boundary conditions, and the inversion systems. The regional transport accounts for the largest part of the discrepancies in the optimized fluxes as well as in the estimation of CO₂ concentration. Temporal and spatial differences in posterior fluxes are consistent with the differences in simulated CO₂ concentration sampled with STILT and FLEXPART over the station network. They demonstrate a spatial pattern over certain areas during June and December suggesting rather systematic differences between STILT and FLEXPART. The differences in the 195 regional transport are mainly caused by the transport schemes, while meteorological forcing data partially contribute to these differences, especially during the months in which net release of CO₂ occurs. However, the differences in CO₂ simulations did not show large sensitivities to other parameters such as the way the surface layer height (maximum altitude considered sensitive to the fluxes in Lagrangian models) and the mixing height are defined. In addition, the global transport models used

Deleted: is likely responsible for the

Deleted: .

Deleted: Our results also suggest that

Deleted: lead to a non-negligible impact

Deleted: to assess the impact of atmospheric transport on inverse modeling estimates. The difference between min

Deleted: The standard deviation of the ensemble members amounted to 0.30 PgC yr⁻¹. We found that...

Deleted: transport model uncertainties lead to large spatial and temporal discrepancies in the optimized fluxes

Formatted: Subscript

Deleted: of

Deleted: However, t

Deleted: Furthermore, the variable magnitude of differences in prior concentrations also reflect the random errors of models to represent the atmospheric mesoscale motion over the receptor locations. The findings outline that the largest part of the differences is predominantly caused by differences in the estimation of CO₂ mixing by the transport models. ...M M

Deleted: M

Deleted: y

|220 in the global inversions that provide the far field contributions to the regional domain are responsible for small, but non-negligible differences in the inversion estimates. These differences appeared to be homogeneous spatially and temporally, which can be considered as bias-like. The differences arising from using different inversion systems integrated over the entire domain of Europe were on the contrary rather small, once differences such as the transport model and the uncertainties are controlled for. However, such an impact is partially a result of applying different structure and shape in the prior flux
|225 uncertainty, while the rest may be attributed to differences in the cost function convergence to reach the minimum. This reflects the importance of the way the uncertainty is prescribed in the tracer inversion systems.

| The divergence in CO₂ flux estimates resulting from swapping the regional transport model emphasizes the need for further
| evaluation of atmospheric transport models in order to improve the performance of the models. At the same time, it is
| important to realistically account for the transport errors in the tracer inversions. Errors in meteorology parameters
|230 assimilated in transport models as forcing data should also be accounted for explicitly, potentially through making use of an ensemble of meteorology data to estimate such errors. Despite the non-negligible difference between inversion systems, this study indicates the importance of following a common inversion protocol when reporting flux estimates from different inversion frameworks.

|235

Code and data availability

The simulations of the ensemble of inversions (posterior NEE calculated using CSR and LUNIA), their respective prior fluxes, and codes can be made available upon request to the corresponding author. The atmospheric datasets of CO₂ dry mole fractions are available at the ICOS Carbon Portal and can be accessed from <https://doi.org/10.18160/ERE9-9D85> (Drought
|240 2018 Team and ICOS Atmosphere Thematic Centre, 2020).

Competing interests

At least one of the (co-)authors is a member of the editorial board of Atmospheric Chemistry and Physics. The peer-review process was guided by an independent editor, and the authors also have no other competing interests to declare.

|245

Acknowledgements

The authors thank Mathias Göckede for his valuable comments on the manuscript in the internal review. SM, CG, CR, and F-T K, acknowledge the computational support of Deutsches Klimarechenzentrum (DKRZ) where the CSR inversion system is implemented. The computations of LUMIA were enabled by resources provided by the Swedish National Infrastructure

|250 for Computing (SNIC) at NSC, partially funded by the Swedish Research Council through grant agreement no. 2018-05973. The authors acknowledge the use of the atmospheric dataset of CO₂ dry mole fractions collected throughout ICOS and NOAA site network.

Deleted: z

1255 **Financial support**

This research has been supported by Horizon 2020 (VERIFY (grant no. 776810) [and CoCO2 \(grant no. 958927\)](#)).

6 References

Babenhauserheide, A., Basu, S., Houweling, S., Peters, W., and Butz, A.: Comparing the CarbonTracker and TM5-4DVar data assimilation systems for CO₂ surface flux inversions, *Atmospheric Chemistry and Physics*, 15, 9747-9763, 10.5194/acp-15-9747-2015, 2015.

Baker, D. F., Law, R. M., Gurney, K. R., Rayner, P., Peylin, P., Denning, A. S., Bousquet, P., Bruhwiler, L., Chen, Y. H., Ciais, P., Fung, I. Y., Heimann, M., John, J., Maki, T., Maksyutov, S., Masarie, K., Prather, M., Pak, B., Taguchi, S., and Zhu, Z.: TransCom 3 inversion intercomparison: Impact of transport model errors on the interannual variability of regional CO₂ fluxes, 1988-2003, *Global Biogeochemical Cycles*, 20, Artn Gb1002 10.1029/2004gb002439, 2006.

Bastos, A., Ciais, P., Friedlingstein, P., Sitch, S., Pongratz, J., Fan, L., Wigneron, J. P., Weber, U., Reichstein, M., Fu, Z., Anthoni, P., Arneth, A., Haverd, V., Jain, A. K., Joetzjer, E., Knauer, J., Lienert, S., Loughran, T., McGuire, P. C., Tian, H., Viovy, N., and Zehle, S.: Direct and seasonal legacy effects of the 2018 heat wave and drought on European ecosystem productivity, *Science Advances*, 6, eaba2724, doi:10.1126/sciadv.aba2724, 2020.

Bousquet, P., Ciais, P., Peylin, P., Ramonet, M., and Monfray, P.: Inverse modeling of annual atmospheric CO₂ sources and sinks: 1. Method and control inversion, *Journal of Geophysical Research: Atmospheres*, 104, 26161-26178, <https://doi.org/10.1029/1999JD900342>, 1999.

Broquet, G., Chevallier, F., Breon, F. M., Kadygrov, N., Alemanno, M., Apadula, F., Hammer, S., Haszpra, L., Meinhardt, F., Morgui, J. A., Necki, J., Piacentino, S., Ramonet, M., Schmid, M., Thompson, R. L., Vermeulen, A. T., Yver, C., and Ciais, P.: Regional inversion of CO₂ ecosystem fluxes from atmospheric measurements: reliability of the uncertainty estimates, *Atmospheric Chemistry and Physics*, 13, 9039-9056, 10.5194/acp-13-9039-2013, 2013.

Chen, H. W., Zhang, F. Q., Lauvaux, T., Davis, K. J., Feng, S., Butler, M. P., and Alley, R. B.: Characterization of Regional-Scale CO₂ Transport Uncertainties in an Ensemble with Flow-Dependent Transport Errors, *Geophysical Research Letters*, 46, 4049-4058, 10.1029/2018gl081341, 2019.

Chevallier, F., Wang, T., Ciais, P., Maignan, F., Bocquet, M., Arain, M. A., Cescatti, A., Chen, J. Q., Dolman, A. J., Law, B. E., Margolis, H. A., Montagnani, L., and Moors, E. J.: What eddy-covariance measurements tell us about prior land flux errors in CO₂-flux inversion schemes, *Global Biogeochemical Cycles*, 26, Artn Gb1021 10.1029/2010gb003974, 2012.

Davies, T.: Lateral boundary conditions for limited area models, *Quarterly Journal of the Royal Meteorological Society*, 140, 185-196, 10.1002/qj.2127, 2014.

Deng, A. J., Lauvaux, T., Davis, K. J., Gaudet, B. J., Miles, N., Richardson, S. J., Wu, K., Sarmiento, D. P., Hardesty, R. M., Bonin, T. A., Brewer, W. A., and Gurney, K. R.: Toward reduced transport errors in a high resolution urban CO₂ inversion system, *Elementa-Sci Anthrop.*, 5, ARTN 20 10.1525/elementa.133, 2017.

Engelen, R. J.: On error estimation in atmospheric CO₂ inversions, *Journal of Geophysical Research*, 107, 10.1029/2002jd002195, 2002.

Eting, I. G., and Newsam, G. N.: Inverse Problems in Atmospheric Constituent Studies .2. Sources in the Free Atmosphere, *Inverse Probl.*, 6, 349-362, Doi 10.1088/0266-5611/6/3/005, 1990.

Fletcher, S. E. M., Gruber, N., Jacobson, A. R., Gloor, M., Doney, S. C., Dutkiewicz, S., Gerber, M., Follows, M., Joos, F., Lindsay, K., Menemenlis, D., Mouchet, A., Muller, S. A., and Sarmiento, J. L.: Inverse estimates of the oceanic sources and sinks of natural CO₂ and the implied oceanic carbon transport, *Global Biogeochemical Cycles*, 21, Artn Gb1010 10.1029/2006gb002751, 2007.

Friedlingstein, P., Jones, M. W., O'Sullivan, M., Andrew, R. M., Bakker, D. C. E., Hauck, J., Le Quéré, C., Peters, G. P., Peters, W., Pongratz, J., Sitch, S., Canadell, J. G., Ciais, P., Jackson, R. B., Alin, S. R., Anthoni, P., Bates, N. R., Becker, M., Bellouin, N., Bopp, L., Chau, T. T. T., Chevallier, F., Chini, L. P., Cronin, M., Currie, K. I., Decharme, B., Djedoutchouang, L. M., Dou, X., Evans, W., Feely, R. A., Feng, L., Gasser, T., Gilfillan, D., Grkitalis, T., Grassi, G., Gregor, L., Gruber, N., Gürses, Ö., Harris, I., Houghton, R. A., Hurtt, G. C., Iida, Y., Ilyina, T., Luijckx, I. T., Jain, A., Jones, S. D., Kato, E., Kennedy, D., Klein Goldevijk, K., Knauer, J., Korsbakken, J. I., Körtzinger, A., Landschützer, P., Lauvset, S. K., Lefèvre, N., Lienert, S., Liu, J., Marland, G., McGuire, P. C., Melton, J. R., Munro, D. R., Nabel, J. E. M. S., Nakaoka, S. I., Niwa, Y., Ono, T., Pierrot, D., Poulter, B., Rehder, G., Resplandy, L., Robertson, E., Rödenbeck, C., Rosan, T. M., Schwinger, J., Schwingshackl, C., Seférian, R., Sutton, A. J., Sweeney, C., Tanhua, T., Tans, P. P., Tian, H., Tilbrook, B.,

1305 Tubiello, F., van der Werf, G. R., Vuichard, N., Wada, C., Wanninkhof, R., Watson, A. J., Willis, D., Wiltshire, A. J., Yuan, W., Yue, C.,
 Yue, X., Zachele, S., and Zeng, J.: Global Carbon Budget 2021, *Earth Syst. Sci. Data*, 14, 1917-2005, 10.5194/essd-14-1917-2022, 2022.

1310 Geels, C., Gloor, M., Ciais, P., Bousquet, P., Peylin, P., Vermeulen, A. T., Dargaville, R., Aalto, T., Brandt, J., Christensen, J. H., Frohn,
 L. M., Haszpra, L., Karstens, U., Rödenbeck, C., Ramonet, M., Carboni, G., and Santaguida, R.: Comparing atmospheric transport models
 for future regional inversions over Europe - Part 1: mapping the atmospheric CO₂ signals, *Atmospheric Chemistry and Physics*, 7, 3461-
 3479, DOI 10.5194/acp-7-3461-2007, 2007.

1315 Gerbig, C., Kornet, S., and Lin, J. C.: Vertical mixing in atmospheric tracer transport models: error characterization and propagation,
Atmospheric Chemistry and Physics, 8, 591-602, DOI 10.5194/acp-8-591-2008, 2008.

Gurney, K. R., Law, R. M., Denning, A. S., Rayner, P. J., Baker, D., Bousquet, P., Bruhwiler, L., Chen, Y.-H., Ciais, P., Fan, S., Fung, I.
 Y., Gloor, M., Heimann, M., Higuchi, K., John, J., Kowalczyk, E., Maki, T., Maksyutov, S., Peylin, P., Prather, M., Pak, B. C., Sarmiento,
 J., Taguchi, S., Takahashi, T., and Yuen, C.-W.: TransCom 3 CO₂ inversion intercomparison: I. Annual mean control results and
 sensitivity to transport and prior flux information, *Tellus B: Chemical and Physical Meteorology*, 55, 555-579,
 10.3402/tellusb.v55i2.16728, 2016.

Kaminski, T., Rayner, P. J., Heimann, M., and Enting, I. G.: On aggregation errors in atmospheric transport inversions, *Journal of
 Geophysical Research: Atmospheres*, 106, 4703-4715, 2001.

1320 Karion, A., Lauvaux, T., Coto, I. L., Sweeney, C., Mueller, K., Gourdjii, S., Angevine, W., Barkley, Z., Deng, A. J., Andrews, A., Stein,
 A., and Whetstone, J.: Intercomparison of atmospheric trace gas dispersion models: Barnett Shale case study, *Atmospheric Chemistry and
 Physics*, 19, 2561-2576, 10.5194/acp-19-2561-2019, 2019.

Kountouris, P., Gerbig, C., Totsche, K. U., Dolman, A. J., Meesters, A. G. C. A., Broquet, G., Maignan, F., Gioli, B., Montagnani, L., and
 Helfter, C.: An objective prior error quantification for regional atmospheric inverse applications, *Biogeosciences*, 12, 7403-7421, DOI
 10.5194/bg-12-7403-2015, 2015.

1325 Kountouris, P., Gerbig, C., Rödenbeck, C., Karstens, U., Koch, T. F., and Heimann, M.: Atmospheric CO₂ inversions on the mesoscale
 using data-driven prior uncertainties: quantification of the European terrestrial CO₂ fluxes, *Atmos. Chem. Phys.*, 18, 3047-3064,
 10.5194/acp-18-3047-2018, 2018a.

1330 Kountouris, P., Gerbig, C., Rödenbeck, C., Karstens, U., Koch, T. F., and Heimann, M.: Technical Note: Atmospheric CO₂ inversions on
 the mesoscale using data-driven prior uncertainties: methodology and system evaluation, *Atmos. Chem. Phys.*, 18, 3027-3045,
 10.5194/acp-18-3027-2018, 2018b.

Lauvaux, T., Miles, N. L., Deng, A. J., Richardson, S. J., Cambaliza, M. O., Davis, K. J., Gaudet, B., Gurney, K. R., Huang, J. H.,
 O'Keefe, D., Song, Y., Karion, A., Oda, T., Patarasuk, R., Razlivanov, I., Sarmiento, D., Shepson, P., Sweeney, C., Turnbull, J., and Wu,
 K.: High-resolution atmospheric inversion of urban CO₂ emissions during the dormant season of the Indianapolis Flux Experiment
 (INFLUX), *J Geophys Res-Atmos.*, 121, 5213-5236, 10.1002/2015jd024473, 2016.

1335 Le Quéré, C., Andrew, R. M., Friedlingstein, P., Sitch, S., Hauck, J., Pongratz, J., Pickers, P. A., Korsbakken, J. I., Peters, G. P., Canadell,
 J. G., Arneth, A., Arora, V. K., Barbero, L., Bastos, A., Bopp, L., Chevallier, F., Chini, L. P., Ciais, P., Doney, S. C., Gkritzalis, T., Goll,
 D. S., Harris, I., Haverd, V., Hoffman, F. M., Hoppema, M., Houghton, R. A., Hurtt, G., Ilyina, T., Jain, A. K., Johannessen, T., Jones, C.,
 D., Kato, E., Keeling, R. F., Goldejwijk, K. K., Landschützer, P., Lefèvre, N., Lierner, S., Liu, Z., Lombardozzi, D., Metzl, N., Munro, D.,
 R., Nabel, J. E. M. S., Nakao, S., Neill, C., Olsen, A., Ono, T., Patra, P., Peregon, A., Peters, W., Peylin, P., Pfelz, B., Pierrot, D.,
 Poulet, B., Rehder, G., Resplandy, L., Robertson, E., Rocher, M., Rödenbeck, C., Schuster, U., Schwinger, J., Séférian, R., Skjelvan, I.,
 Steinhoff, T., Sutton, A., Tans, P. P., Tian, H., Tilbrook, B., Tubiello, F. N., van der Laan-Luijkx, I. T., van der Werf, G. R., Viovy, N.,
 Walker, A. P., Wiltshire, A. J., Wright, R., Zachele, S., and Zheng, B.: Global Carbon Budget 2018, *Earth Syst. Sci. Data*, 10, 2141-2194,
 10.5194/essd-10-2141-2018, 2018.

1340 Lin, J. C., Gerbig, C., Wofsy, S. C., Andrews, A. E., Daube, B. C., Davis, K. J., and Grainger, C. A.: A near-field tool for simulating the
 upstream influence of atmospheric observations: The Stochastic Time-Inverted Lagrangian Transport (STILT) model, *J Geophys Res-
 Atmos.*, 108, Artm 4493, 10.1029/2002jd003161, 2003.

1345 Liu, J. J., Fung, I., Kalnay, E., and Kang, J. S.: CO₂ transport uncertainties from the uncertainties in meteorological fields, *Geophysical
 Research Letters*, 38, Artm L12808, 10.1029/2011gl047213, 2011.

Mahadevan, P., Wofsy, S. C., Matross, D. M., Xiao, X. M., Dunn, A. L., Lin, J. C., Gerbig, C., Munger, J. W., Chow, V. Y., and Gottlieb,
 E. W.: A satellite-based biosphere parameterization for net ecosystem CO₂ exchange: Vegetation Photosynthesis and Respiration Model
 (VPRM), *Global Biogeochemical Cycles*, 22, Artm Gb2005, 10.1029/2006gb002735, 2008.

1350 Monteil, G., Broquet, G., Scholze, M., Lang, M., Karstens, U., Gerbig, C., Koch, F. T., Smith, N. E., Thompson, R. L., Luijkx, I. T.,
 White, E., Meesters, A., Ciais, P., Ganesan, A. L., Manning, A., Mischirow, M., Peters, W., Peylin, P., Tarniewicz, J., Rigby, M.,
 Rödenbeck, C., Vermeulen, A., and Walton, E. M.: The regional European atmospheric transport inversion comparison, EUROCOM: first
 results on European-wide terrestrial carbon fluxes for the period 2006–2015, *Atmos. Chem. Phys.*, 20, 12063-12091, 10.5194/acp-20-
 12063-2020, 2020.

Monteil, G., and Scholze, M.: Regional CO₂ inversions with LUMIA, the Lund University Modular Inversion Algorithm, v1.0, *Geosci. Model Dev.*, 14, 3383-3406, 10.5194/gmd-14-3383-2021, 2021.

Munassar, S., Rödenbeck, C., Koch, F. T., Totsche, K. U., Galkowski, M., Walther, S., and Gerbig, C.: Net ecosystem exchange (NEE) estimates 2006–2019 over Europe from a pre-operational ensemble-inversion system, *Atmos. Chem. Phys.*, 22, 7875-7892, 10.5194/acp-22-7875-2022, 2022.

1365 Petrescu, A. M. R., McGrath, M. J., Andrew, R. M., Peylin, P., Peters, G. P., Ciais, P., Broquet, G., Tubiello, F. N., Gerbig, C., Pongratz, J., Janssens-Maenhout, G., Grassi, G., Nabuurs, G. J., Regnier, P., Lauerwald, R., Kuhnert, M., Balkovič, J., Schellhaas, M. J., Denier van der Gon, H. A. C., Solazzo, E., Qiu, C., Pilli, R., Konovalov, I. B., Houghton, R. A., Günther, D., Perugini, L., Crippa, M., Ganzennmüller, R., Luijckx, I. T., Smith, P., Munassar, S., Thompson, R. L., Conchedda, G., Monteil, G., Scholze, M., Karstens, U., Brockmann, P., and Dolman, A. J.: The consolidated European synthesis of CO₂ emissions and removals for the European Union and United Kingdom: 1990–2018, *Earth Syst. Sci. Data*, 13, 2363-2406, 10.5194/essd-13-2363-2021, 2021.

Peylin, P., Baker, D., Sarmiento, J., Ciais, P., and Bousquet, P.: Influence of transport uncertainty on annual mean and seasonal inversions of atmospheric CO₂ data, *J Geophys Res-Atmos*, 107, ArtN 4385 10.1029/2001jd000857, 2002.

1370 1375 Pissos, I., Sollum, E., Grythe, H., Kristiansen, N. I., Cassiani, M., Eckhardt, S., Arnold, D., Morton, D., Thompson, R. L., Groot Zwaaftink, C. D., Evangelou, N., Sodemann, H., Haimberger, L., Henne, S., Brunner, D., Burkhart, J. F., Fouilloux, A., Brioude, J., Philipp, A., Seibert, P., and Stohl, A.: The Lagrangian particle dispersion model FLEXPART version 10.4, *Geosci. Model Dev.*, 12, 4955-4997, 10.5194/gmd-12-4955-2019, 2019.

Rivier, L., Peylin, P., Ciais, P., Gloor, M., Rödenbeck, C., Geels, C., Karstens, U., Bousquet, P., Brandt, J., and Heimann, M.: European CO₂ fluxes from atmospheric inversions using regional and global transport models, *Climatic Change*, 103, 93-115, 10.1007/s10584-010-9908-4, 2010.

Rödenbeck, C., Houweling, S., Gloor, M., and Heimann, M.: CO₂ flux history 1982–2001 inferred from atmospheric data using a global inversion of atmospheric transport, *Atmos. Chem. Phys.*, 3, 1919-1964, 10.5194/acp-3-1919-2003, 2003.

1380 1385 Rödenbeck, C.: Estimating CO₂ sources and sinks from atmospheric mixing ratio measurements using a global inversion of atmospheric transport, 06, 2005.

Rödenbeck, C., Gerbig, C., Trusilova, K., and Heimann, M.: A two-step scheme for high-resolution regional atmospheric trace gas inversions based on independent models, *Atmos. Chem. Phys.*, 9, 5331-5342, 10.5194/acp-9-5331-2009, 2009.

Rödenbeck, C., Zaelke, S., Keeling, R., and Heimann, M.: The European carbon cycle response to heat and drought as seen from atmospheric CO₂ data for 1999–2018, *Philos Trans R Soc Lond B Biol Sci*, 375, 20190506, 10.1098/rstb.2019.0506, 2020.

1390 1395 Roedenbeck, C., Gerbig, C., Trusilova, K., and Heimann, M.: A two-step scheme for high-resolution regional atmospheric trace gas inversions based on independent models, *Atmos. Chem. Phys.*, 9, 5331-5342, 2009.

Schuh, A. E., Jacobson, A. R., Basu, S., Weir, B., Baker, D., Bowman, K., Chevalier, F., Crowell, S., Davis, K. J., Deng, F., Denning, S., Feng, L., Jones, D., Liu, J. J., and Palmer, P. I.: Quantifying the Impact of Atmospheric Transport Uncertainty on CO₂ Surface Flux Estimates, *Global Biogeochemical Cycles*, 33, 484-500, 10.1029/2018gb006086, 2019.

1400 1405 Shi, H., Tian, H. Q., Pan, N. Q., Reyer, C. P. O., Ciais, P., Chang, J. F., Forrest, M., Frieler, K., Fu, B. J., Gadeke, A., Hickler, T., Ito, A., Ostberg, S., Pan, S. F., Stevanovic, M., and Yang, J.: Saturation of Global Terrestrial Carbon Sink Under a High Warming Scenario, *Global Biogeochemical Cycles*, 35, ARTN e2020GB006800, 2021.

Steinbach, J., Gerbig, C., Rödenbeck, C., Karstens, U., Minejima, C., and Mukai, H.: The CO₂ release and Oxygen uptake from Fossil Fuel Emission Estimate (COFFEE) dataset: effects from varying oxidative ratios, *Atmos. Chem. Phys.*, 11, 6855-6870, 10.5194/acp-11-6855-2011, 2011.

Thompson, R. L., Broquet, G., Gerbig, C., Koch, T., Lang, M., Monteil, G., Munassar, S., Nickless, A., Scholze, M., Ramonet, M., Karstens, U., van Schaik, E., Wu, Z., and Rodenbeck, C.: Changes in net ecosystem exchange over Europe during the 2018 drought based on atmospheric observations, *Philos Trans R Soc Lond B Biol Sci*, 375, 20190512, 10.1098/rstb.2019.0512, 2020.

Tolk, L. F., Meesters, A. G. C. A., Dolman, A. J., and Peters, W.: Modelling representation errors of atmospheric CO₂ mixing ratios at a regional scale, *Atmospheric Chemistry and Physics*, 8, 6587-6596, DOI 10.5194/acp-8-6587-2008, 2008.

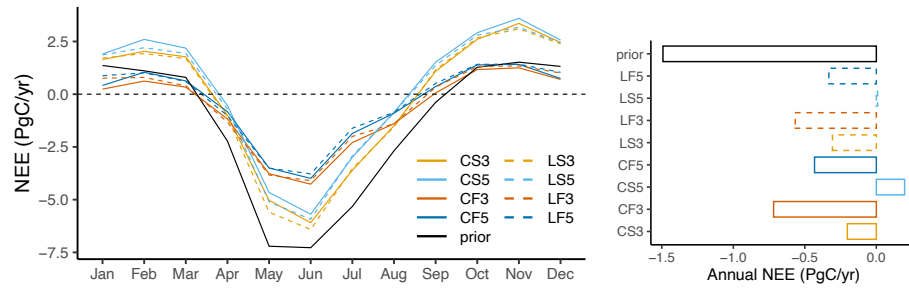


Figure 1: Left panel refers to posterior monthly NEE estimated using eight inversions, including prior NEE shown in black colour, with CSR (solid lines) and LUMIA (dashed lines), and right panel denotes the corresponding annually aggregated fluxes. Orange and red colours correspond to TM3 and dark/light blue to TM5. Orange and light blue colours refer to STILT and red and dark blue to FLEXPART.

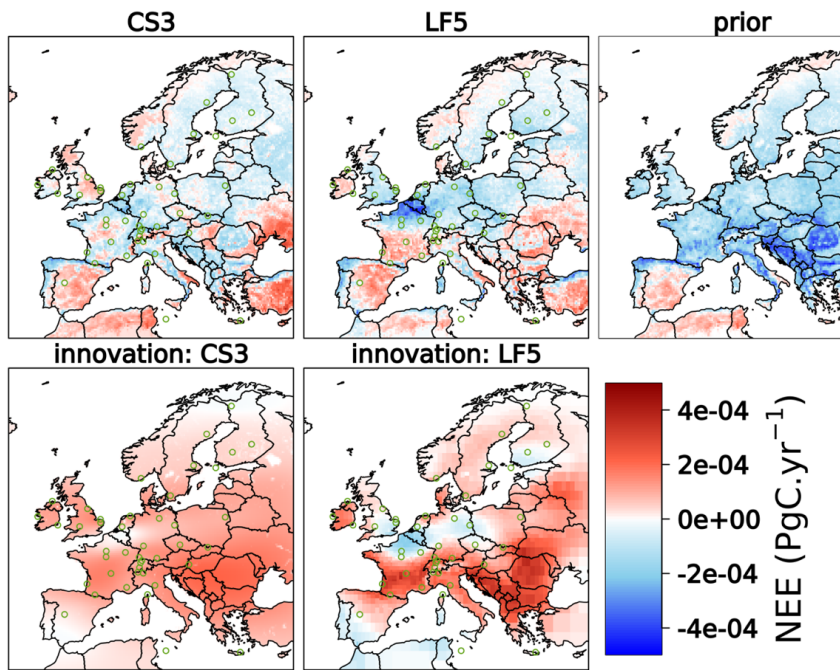


Figure 2: First row shows the spatial distributions of annual NEE estimated with the base inversions CS3 and LF5, as well as their prior. Second row depicts the innovations of fluxes calculated for the inversions CS3, LF5. Green circles denote the locations of observational sites.

1425

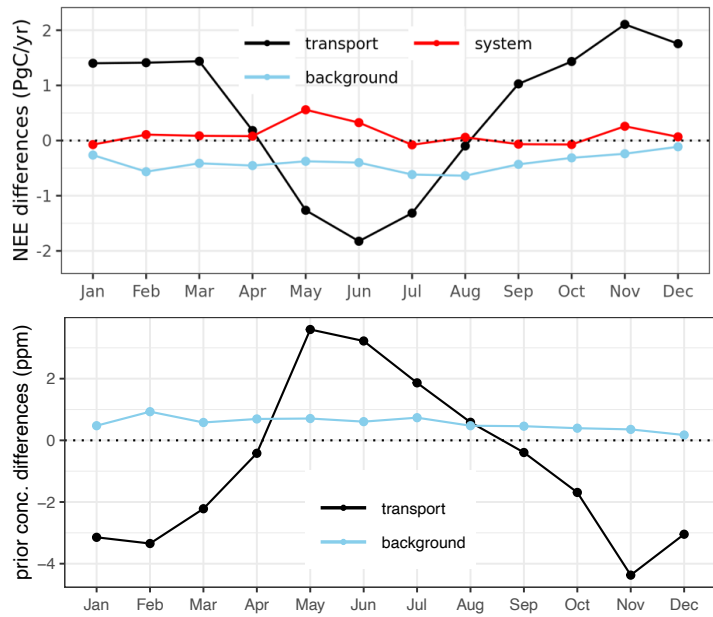


Figure 3: Differences in optimized fluxes (top) and prior concentrations (bottom) calculated with the regional transport models STILT and FLEXPART (CS3-CF3) and background provided through TM3 and TM5 (CS3-CS5). "system" refers to the differences between CSR and LUMIA inversion for optimized fluxes (CS5-LS5).

1430

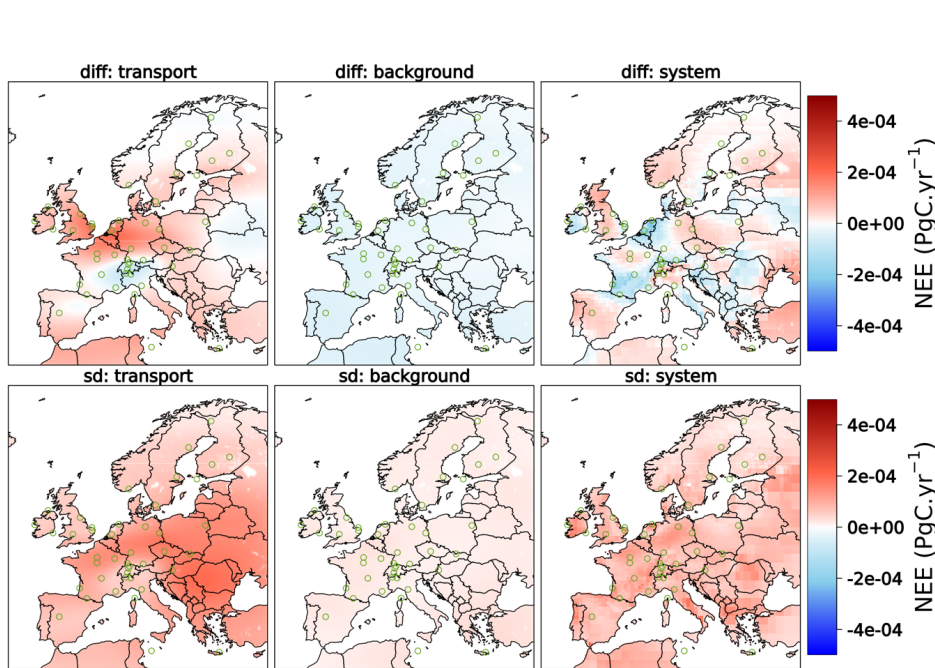


Figure 4: First row indicates differences in annual posterior NEE estimated with STILT and FLEXPART models referred to as “transport” (CS3-CF3), TM3 and TM5 referred to as “background” (CS3-CS5), and CSR and LUMIA referred to as “system” (CF3-LF3); second row demonstrates the standard deviations of the corresponding monthly differences.

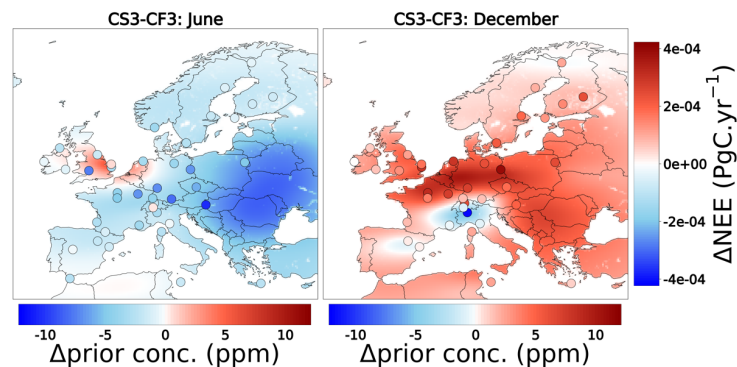
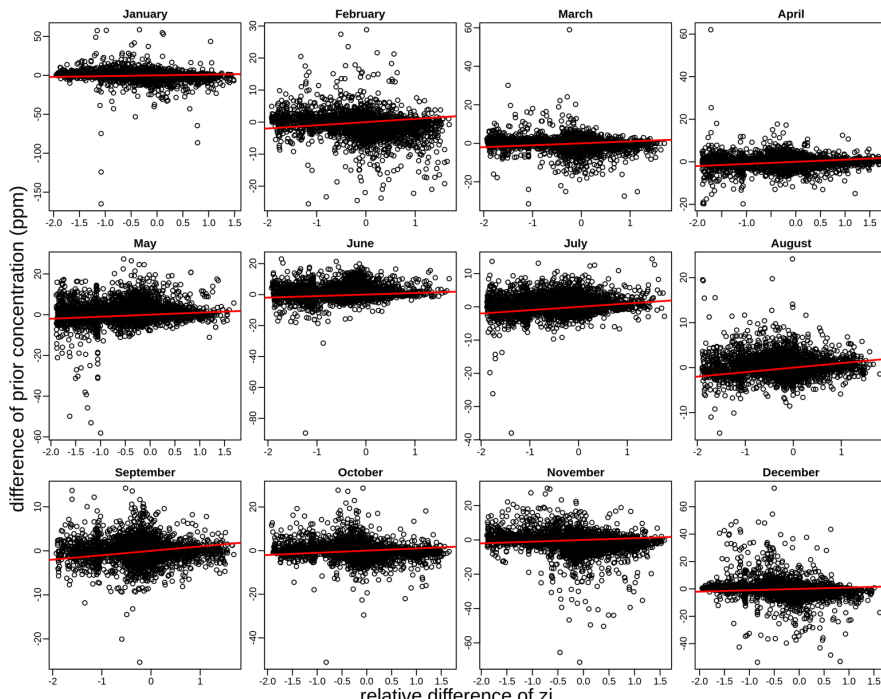
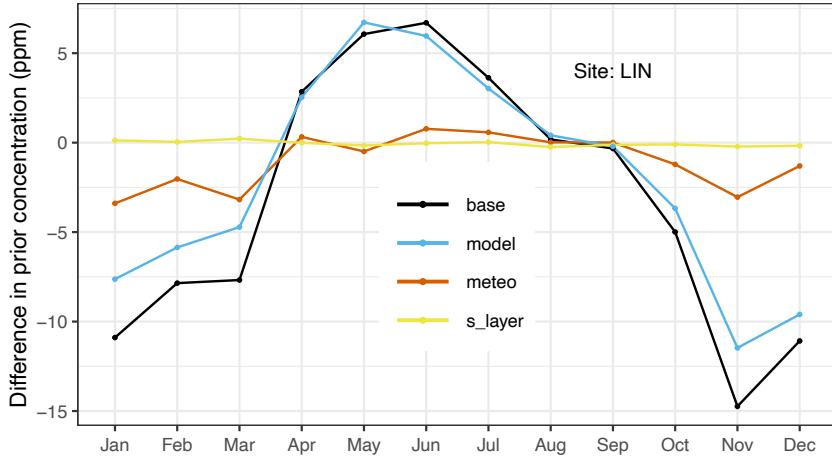


Figure 5: Spatial differences of posterior NEE estimated from the inversions CS3 and CF3 with STILT and FLEXPART transport models during June and December; filled circles indicate the differences in prior concentrations at the locations of sites (horizontal legend explains the magnitude of differences).

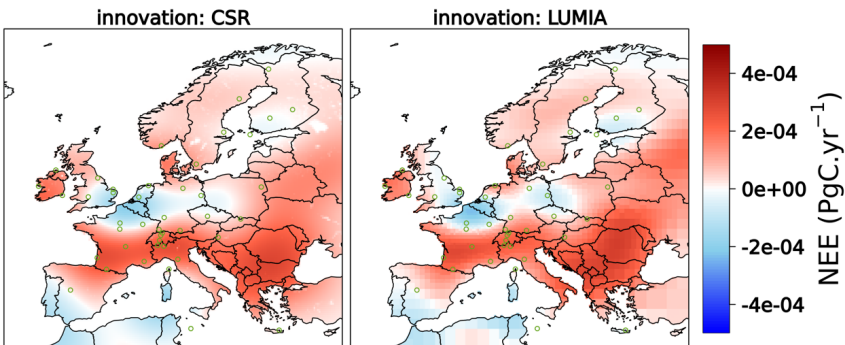


1440

Figure 6: Scatter plot of differences of prior concentrations and mixing heights calculated with STILT and FLEXPART models (i.e., STILT-FLEXPART on the x- and the y-axis). Red lines indicate the slopes.



1445 Figure 7: Differences in prior concentration simulated at LIN with STILT and FLEXPART using different configurations.
 1450 "s_layer", yellow line, refers to the difference calculated with STILT using two assumptions of defining the surface layer height, once with the default as 0.5 of the mixed layer, and once with 100 m as used in FLEXPART. "meteo", red line, indicates the differences calculated with FLEXPART using two different types of meteorological data, IFS (the STILT default) and ERA-5. "model", blue line, denotes the differences calculated with STILT and FLEXPART, given identical meteorological data (IFS) and surface layer height (100 m). "base", black line, refers to the base configurations of STILT and FLEXPART encompassing all possible differences between models - i.e., 1) STILT with IFS forecasting data and a surface layer height as 0.5 of the mixed layer height, and 2) FLEXPART with ERA-5 reanalysis and the surface layer height of 100 m.



1455 Figure 8: Innovation of fluxes calculated from CSR and LUMIA using identical uncertainties of prior flux and measurements. The uncertainty flux shape was flat and the decaying spatial correlation was fit to Gaussian function with 500 km scale. FLEXPART and TM5 models were used in this experiment.

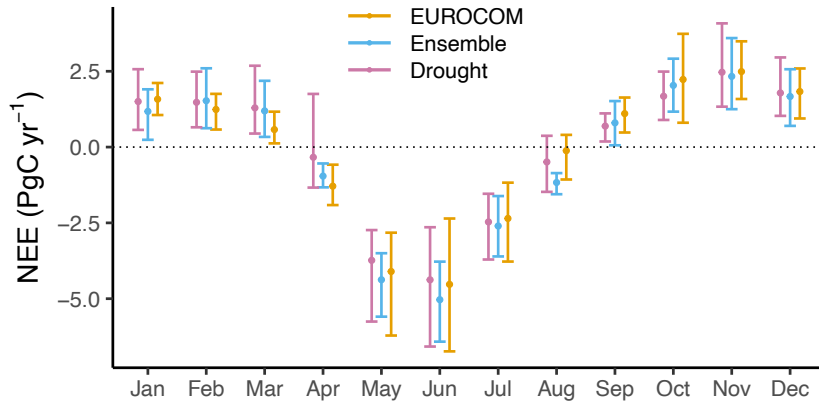


Figure 9: Comparison of monthly NEE estimates calculated as the mean of six inversions taken from Monteil et al. (2020), denoted as “EUROCOM”, eight inversion members conducted in our study (set-ups listed in Table 2), denoted as “Ensemble”, and five inversions used in Thompson et al. (2020) for the 2018 drought study denoted as “Drought”. The error bars refer to the spreads (min/max) over the respective members amid each ensemble of inversions.

1460

1465

1470

1475

Table 1. Atmospheric sites used in the inversions.

Site code	Site name	Coordinates (lat, lon) ^o	STILT release height (magl)	FLEXPART release height (magl)	Time window (UTC)	Uncertainty (ppm)
SM3	Hyytiala	61.85, 24.29	125	125	10:00-14:00	1.5
BI5	Bialystok	53.23, 23.03	300	300	10:00-14:00	1.5
FKL	Finokalia	35.34, 25.67	15	15	10:00-14:00	1.5
PAL	Pallas	67.97, 24.12	12	12	10:00-14:00	2.5
PUI	Puijo	62.91, 27.65	84	84	10:00-14:00	1.5
UTO	Uto Baltic Sea	59.78, 21.37	57	57	10:00-14:00	1.5
BIR	Birkenes Observatory	58.389, 8.25	3	3	11:00-15:00	2.5
BR5	Beromuenster	47.19, 8.17	212	212	11:00-15:00	1.5
DEC	Deltade l'Ebre	40.74, 0.79	10	10	11:00-15:00	1.5
EEC	El_Estrecho	36.0586, -5.664	20	20	11:00-15:00	1.5
GIC	Sierra de Gredos	40.3457, -5.1755	20	20	11:00-15:00	2.5
HEI	Heidelberg	49.417, 8.674	30	30	11:00-15:00	4
HP4	Hohenpeissenberg	47.8011, 11.0246	300	131	11:00-15:00	1.5
ER2	ERSA	42.9692, 9.3801	40	40	11:00-15:00	1.5
HT3	Hyltemossa	56.0969, 13.4189	150	150	11:00-15:00	1.5
HU4	Hegyhatsal Tower	46.95, 16.65	115	115	11:00-15:00	1.5
IP3	Ispra	45.8147, 8.636	100	100	11:00-15:00	1.5
KR3	Kresin	49.572, 15.08	250	250	11:00-15:00	1.5
LMU	La Muela	41.5941, -1.1003	80	79	11:00-15:00	1.5
LMP	Lampedusa	35.53, 12.62	10	10	11:00-15:00	1.5
LUT	Lutjewad	53.4036, 6.3528	60	60	11:00-15:00	2.5
NO3	Norunda	60.0864, 17.4794	100	100	11:00-15:00	1.5
SV3	Svartberget	64.256, 19.775	150	150	11:00-15:00	1.5
TR4	Trainou	47.9647, 2.1125	180	180	11:00-15:00	1.5
OHP	Observatoire de Haute Provence	43.931, 5.712	100	100	11:00-15:00	1.5
SA3	Saclay	48.7227, 2.142	100	100	11:00-15:00	1.5
LHW	Laegern Hochwacht	47.4822, 8.3973	400	32	11:00-15:00	2.5
BS3	Bilsdale	54.359, -1.15	248	248	12:00 -16:00	1.5
RG2	Ridge Hill	51.9976, -2.54	90	90	12:00 -16:00	1.5
TA3	Tacnolestan	52.5177, 1.1386	185	185	12:00 -16:00	1.5
WAO	Weybourne Norfolk	52.9502, 1.1219	10	10	12:00 -16:00	1.5
OP3	OPE_ANDRA	48.5619, 5.5036	120	120	14:00-17:00	1.5
GA5	Gartow	53.0657, 11.4429	341	341	14:00-18:00	1.5
LIN	Lindenberg	52.1663, 14.1226	98	98	14:00-18:00	1.5
BIS	Biscarrose	44.3781, -1.2311	47	47	14:00-18:00	2.5
CRP	Carnoise Point	52.18, -6.37	14	14	14:00-18:00	1.5
MHD	MaceHead	53.3261, -9.9036	24	24	14:00-18:00	1.5
MLH	Marlin Head	55.355, -7.333	47	47	14:00-18:00	1.5
JFJ	Jungfraujoch	46.5475, 7.9851	720	3570	23:00-3:00	1.5
KAS	Kasrprovy Wierch	49.2325, 19.9818	480	1989	23:00-3:00	1.5
PUY	Puy de Dome	45.7719, 2.9658	400	1465	23:00-3:00	1.5

SI2	Schauinsland	47.91, 7.91	450	1205	23:00-3:00	1.5
PTR	Plateau Rosa Station	45.94, 7.71	500	3480	23:00-3:00	1.5
PD2	Pic du Midi	42.9372, 0.1411	1458	2877	23:00-3:00	1.5
CMN	Monte Cimone	44.1963, 10.6999	670	2165	23:00-3:00	1.5

Table 2: List of the inversion set-ups

Inversion system	Transport model	Global boundary condition	Identifier code	Flux Uncertainty	
				Shape	Decay
LUMIA	FLEXPART	TM5	LF5	Variable	Gaussian
LUMIA	FLEXPART	TM3	LF3	Variable	Gaussian
LUMIA	STILT	TM5	LS5	Variable	Gaussian
LUMIA	STILT	TM3	LS3	Variable	Gaussian
CSR	STILT	TM3	CS3	Flat	Hyperbolic
CSR	STILT	TM5	CS5	Flat	Hyperbolic
CSR	FLEXPART	TM3	CF3	Flat	Hyperbolic
CSR	FLEXPART	TM5	CF5	Flat	Hyperbolic

1485

1490

Page 3: [1] Deleted Saqr Munassar 17/11/2022 17:13:00

▼

Page 3: [2] Deleted Saqr Munassar 09/11/2022 13:05:00

▼

Page 3: [3] Deleted Saqr Munassar 09/11/2022 19:48:00

▼

Page 8: [4] Deleted Saqr Munassar 01/11/2022 19:08:00

▼

Page 8: [4] Deleted Saqr Munassar 01/11/2022 19:08:00

▼

Page 8: [4] Deleted Saqr Munassar 01/11/2022 19:08:00

▼

Page 8: [4] Deleted Saqr Munassar 01/11/2022 19:08:00

▼

Page 8: [4] Deleted Saqr Munassar 01/11/2022 19:08:00

▼

Page 8: [4] Deleted Saqr Munassar 01/11/2022 19:08:00

▼

Page 8: [4] Deleted Saqr Munassar 01/11/2022 19:08:00

▼

Page 8: [4] Deleted Saqr Munassar 01/11/2022 19:08:00

▼

Page 8: [4] Deleted Saqr Munassar 01/11/2022 19:08:00

▼

Page 8: [4] Deleted Saqr Munassar 01/11/2022 19:08:00

▼

Page 8: [4] Deleted Saqr Munassar 01/11/2022 19:08:00

▼

Page 8: [4] Deleted Saqr Munassar 01/11/2022 19:08:00

▼

Page 8: [5] Deleted Saqr Munassar 27/10/2022 22:25:00

▼

Page 8: [5] Deleted Saqr Munassar 27/10/2022 22:25:00

▼

Page 8: [5] Deleted Saqr Munassar 27/10/2022 22:25:00

▼

Page 8: [5] Deleted Saqr Munassar 27/10/2022 22:25:00

▼

Page 8: [5] Deleted Saqr Munassar 27/10/2022 22:25:00

▼

Page 8: [5] Deleted Saqr Munassar 27/10/2022 22:25:00

▼

Page 8: [5] Deleted Saqr Munassar 27/10/2022 22:25:00

▼

Page 8: [5] Deleted Saqr Munassar 27/10/2022 22:25:00

▼

Page 8: [5] Deleted Saqr Munassar 27/10/2022 22:25:00

▼

Page 8: [5] Deleted Saqr Munassar 27/10/2022 22:25:00

▼

Page 8: [5] Deleted Saqr Munassar 27/10/2022 22:25:00

▼

Page 8: [5] Deleted Saqr Munassar 27/10/2022 22:25:00

▼

Page 8: [5] Deleted Saqr Munassar 27/10/2022 22:25:00

▼

Page 8: [5] Deleted Saqr Munassar 27/10/2022 22:25:00

▼

Page 8: [5] Deleted Saqr Munassar 27/10/2022 22:25:00

▼

Page 8: [5] Deleted Saqr Munassar 27/10/2022 22:25:00

▼

Page 8: [5] Deleted Saqr Munassar 27/10/2022 22:25:00

▼

Page 8: [6] Deleted Saqr Munassar 27/10/2022 22:56:00

▼

Page 8: [6] Deleted Saqr Munassar 27/10/2022 22:56:00

▼

Page 8: [6] Deleted Saqr Munassar 27/10/2022 22:56:00

▼

Page 8: [6] Deleted Saqr Munassar 27/10/2022 22:56:00

▼

Page 8: [6] Deleted Saqr Munassar 27/10/2022 22:56:00

▼

Page 8: [6] Deleted Saqr Munassar 27/10/2022 22:56:00

▼

Page 8: [6] Deleted Saqr Munassar 27/10/2022 22:56:00

▼

Page 8: [6] Deleted Saqr Munassar 27/10/2022 22:56:00

▼

Page 8: [6] Deleted Saqr Munassar 27/10/2022 22:56:00

▼

Page 8: [7] Deleted Saqr Munassar 27/10/2022 23:27:00

▼

Page 8: [7] Deleted Saqr Munassar 27/10/2022 23:27:00

▼

Page 8: [7] Deleted Saqr Munassar 27/10/2022 23:27:00

▼

Page 8: [7] Deleted Saqr Munassar 27/10/2022 23:27:00

▼

Page 8: [7] Deleted Saqr Munassar 27/10/2022 23:27:00

▼

Page 8: [8] Deleted Saqr Munassar 27/10/2022 23:49:00

▼

Page 8: [8] Deleted Saqr Munassar 27/10/2022 23:49:00

▼

Page 8: [8] Deleted Saqr Munassar 27/10/2022 23:49:00

▼

Page 8: [8] Deleted Saqr Munassar 27/10/2022 23:49:00

▼.....
Page 9: [12] Deleted **Saqr Munassar** **02/11/2022 10:43:00**

▼.....
Page 9: [13] Deleted **Saqr Munassar** **28/10/2022 13:11:00**

▼.....
Page 10: [14] Deleted **Saqr Munassar** **28/10/2022 13:18:00**

▼.....
Page 10: [15] Deleted **Saqr Munassar** **02/11/2022 12:32:00**

▼.....
Page 10: [16] Deleted **Saqr Munassar** **01/11/2022 12:43:00**

▼.....
Page 11: [17] Deleted **Saqr Munassar** **01/11/2022 16:17:00**

▼.....
Page 11: [17] Deleted **Saqr Munassar** **01/11/2022 16:17:00**

▼.....
Page 11: [17] Deleted **Saqr Munassar** **01/11/2022 16:17:00**

▼.....
Page 11: [17] Deleted **Saqr Munassar** **01/11/2022 16:17:00**

▼.....
Page 11: [17] Deleted **Saqr Munassar** **01/11/2022 16:17:00**

▼.....
Page 11: [17] Deleted **Saqr Munassar** **01/11/2022 16:17:00**

▼.....
Page 11: [18] Deleted **Saqr Munassar** **18/11/2022 12:37:00**

▼.....
Page 11: [18] Deleted **Saqr Munassar** **18/11/2022 12:37:00**

▼.....
Page 11: [18] Deleted **Saqr Munassar** **18/11/2022 12:37:00**

▼.....
Page 11: [18] Deleted **Saqr Munassar** **18/11/2022 12:37:00**

Page 11: [19] Deleted Saqr Munassar 17/11/2022 16:36:00

▼

Page 11: [19] Deleted Saqr Munassar 17/11/2022 16:36:00

▼

Page 11: [19] Deleted Saqr Munassar 17/11/2022 16:36:00

▼

Page 11: [19] Deleted Saqr Munassar 17/11/2022 16:36:00

▼

Page 11: [19] Deleted Saqr Munassar 17/11/2022 16:36:00

▼

Page 11: [19] Deleted Saqr Munassar 17/11/2022 16:36:00

▼

Page 11: [20] Moved to page 11 (Move #3) Saqr Munassar 01/11/2022 16:27:00

▼

1.1

Page 11: [20] Moved to page 11 (Move #3) Saqr Munassar 01/11/2022 16:27:00

▼

1.2

Page 11: [21] Deleted Saqr Munassar 18/11/2022 17:35:00

▼

Page 11: [21] Deleted Saqr Munassar 18/11/2022 17:35:00

▼

Page 11: [21] Deleted Saqr Munassar 18/11/2022 17:35:00

▼

Page 11: [21] Deleted Saqr Munassar 18/11/2022 17:35:00

▼

Page 11: [21] Deleted Saqr Munassar 18/11/2022 17:35:00

▼

Page 11: [21] Deleted Saqr Munassar 18/11/2022 17:35:00

▼

Page 11: [22] Deleted Saqr Munassar 17/11/2022 13:17:00

▼.....
Page 11: [22] Deleted **Saqr Munassar** **17/11/2022 13:17:00**

▼.....
Page 11: [22] Deleted **Saqr Munassar** **17/11/2022 13:17:00**

▼.....
Page 11: [22] Deleted **Saqr Munassar** **17/11/2022 13:17:00**

▼.....
Page 13: [23] Deleted **Saqr Munassar** **02/11/2022 10:50:00**

▼.....
Page 14: [24] Deleted **Saqr Munassar** **02/11/2022 23:45:00**

▼.....
Page 14: [25] Deleted **Saqr Munassar** **18/11/2022 20:25:00**